Supplementary Information

Pressure-constrained Sonication Activation of Flexible Printed Metal-particle Circuit

Lingxiao Cao[1,2], Zhonghao Wang[1,2], Daiwei Hu[1], Haoxuan Dong[1], Chunchun Qu[1], Yi Zheng[1], Chao Yang[1], Rui Zhang[1], Chunxiao Xing[1], Zhen Li[1], Zhe Xin[1], Du Chen[1], Zhenghe Song[1], Zhizhu He[1]✉

[1]Center for Agricultural Flexible Electronics Technology, College of Engineering, China Agricultural University, Beijing 100083, China.

[2]These authors contributed equally

✉ Corresponding author. Email: zzhe@cau.edu.cn

This PDF file includes:

Supplementary Figures 1-44

Supplementary Tables 1-3

Supplementary Notes 1-3

References 1-39

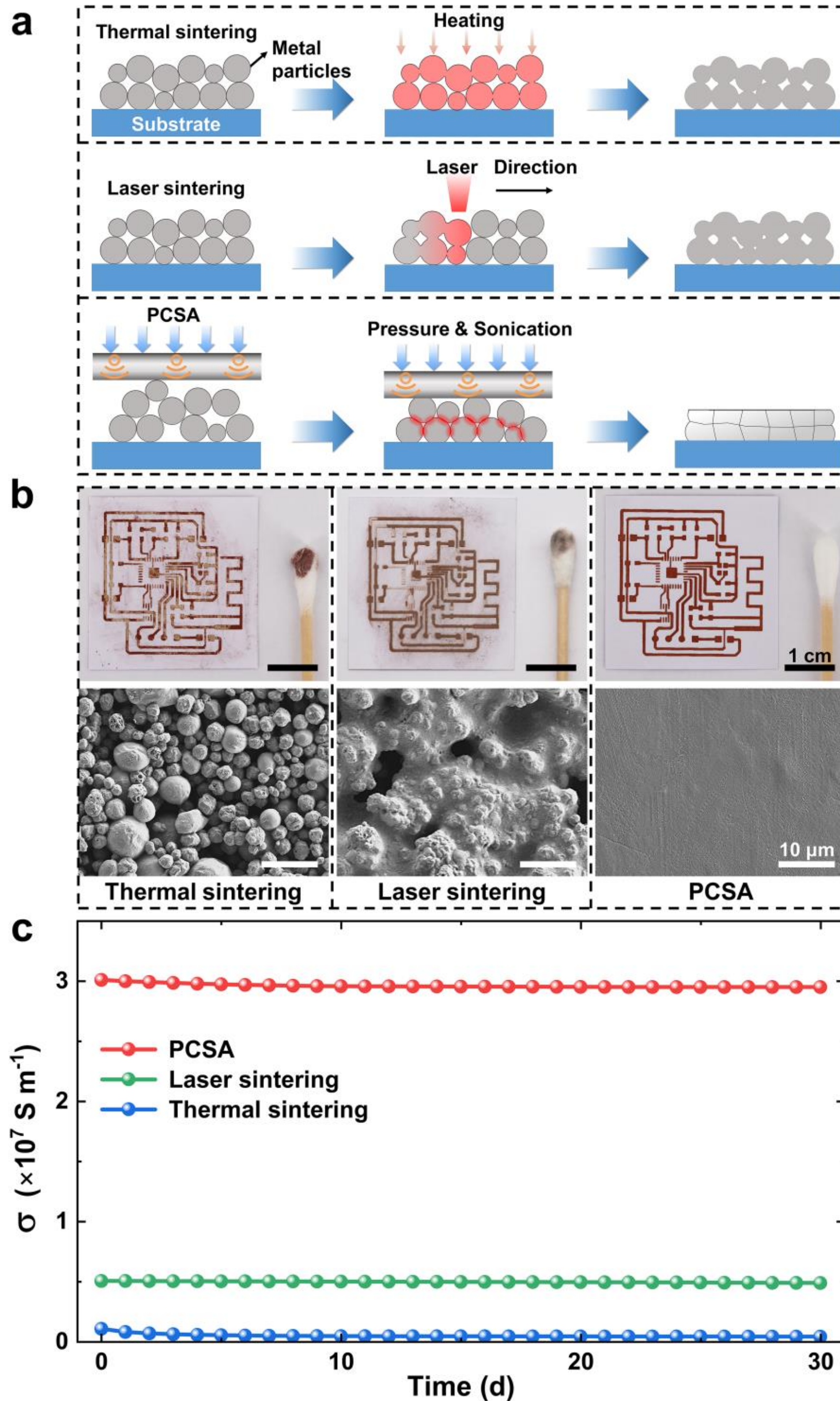

Fig. 1| Comparison of the Cu particle-based printed circuits activated by PCSA, thermal (180 ºC for 30 mins), and laser sintering methods. a, Principle illustration of the postprocessing methods. **b**, The images of the Cu-printed circuits were wiped with a cotton swab, and SEMs of the printed Cu-particle pattern surface after posttreatment methods of thermal sintering, laser sintering, and PCSA (*n* = 3; independent samples). c, The electrical conductivity of the Cu-printed circuits was activated by three methods when exposed to the air for 30 days. The PCSA method can achieve high electrical conductivity of 3.03×10^{7} S/m for printed Cu-microparticle pattern, which is 6 times that (0.50×10^{7} S/m) for laser sintering method and 27.5 times that (0.11×10^{7} S/m) for thermal sintering method, respectively.

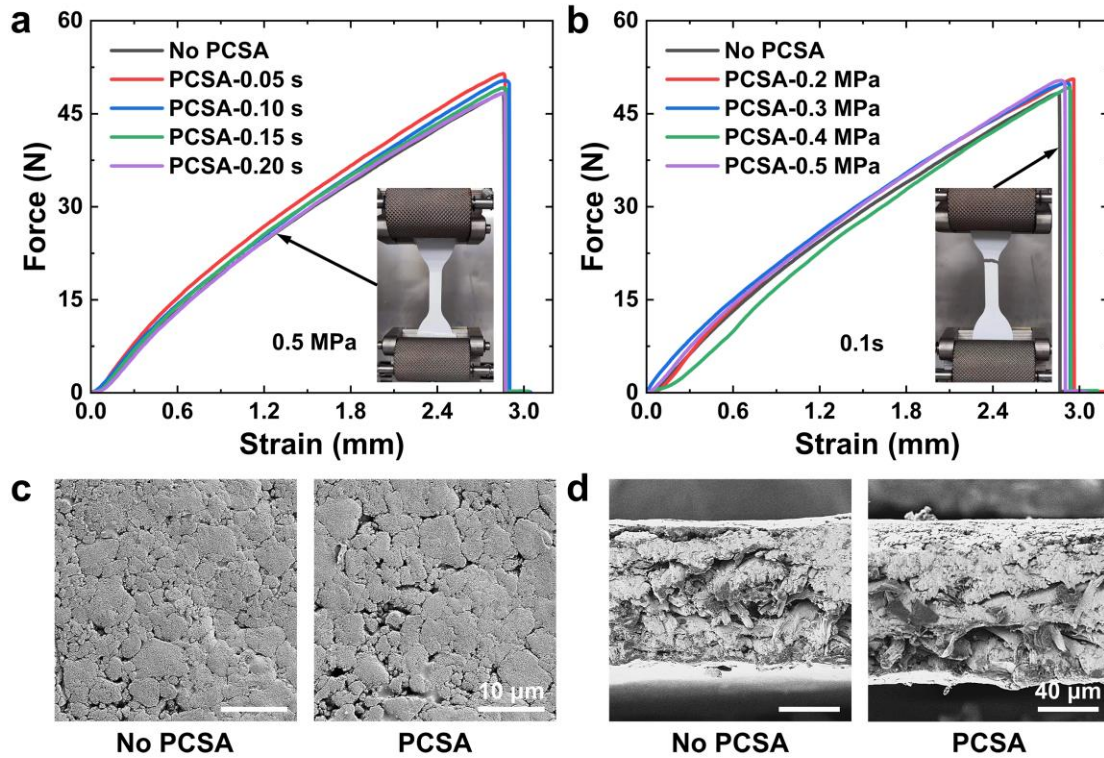

Fig.2| Impacts of the PCSA processing on paper substrate. **a**, Impacts of action time of the PCSA processing (constrained pressure with 0.5 MPa) on the mechanical property of the paper substrate. **b**, Impacts of constrained pressure of the PCSA processing (action time with 0.1 s) on the mechanical property of the paper substrate. SEMs of the surface (**c**) and cross-section area (**d**) before/after the PCSA processing (constrained pressure with 0.5 MPa and action time with 0.1 s) (n = 3; independent samples).

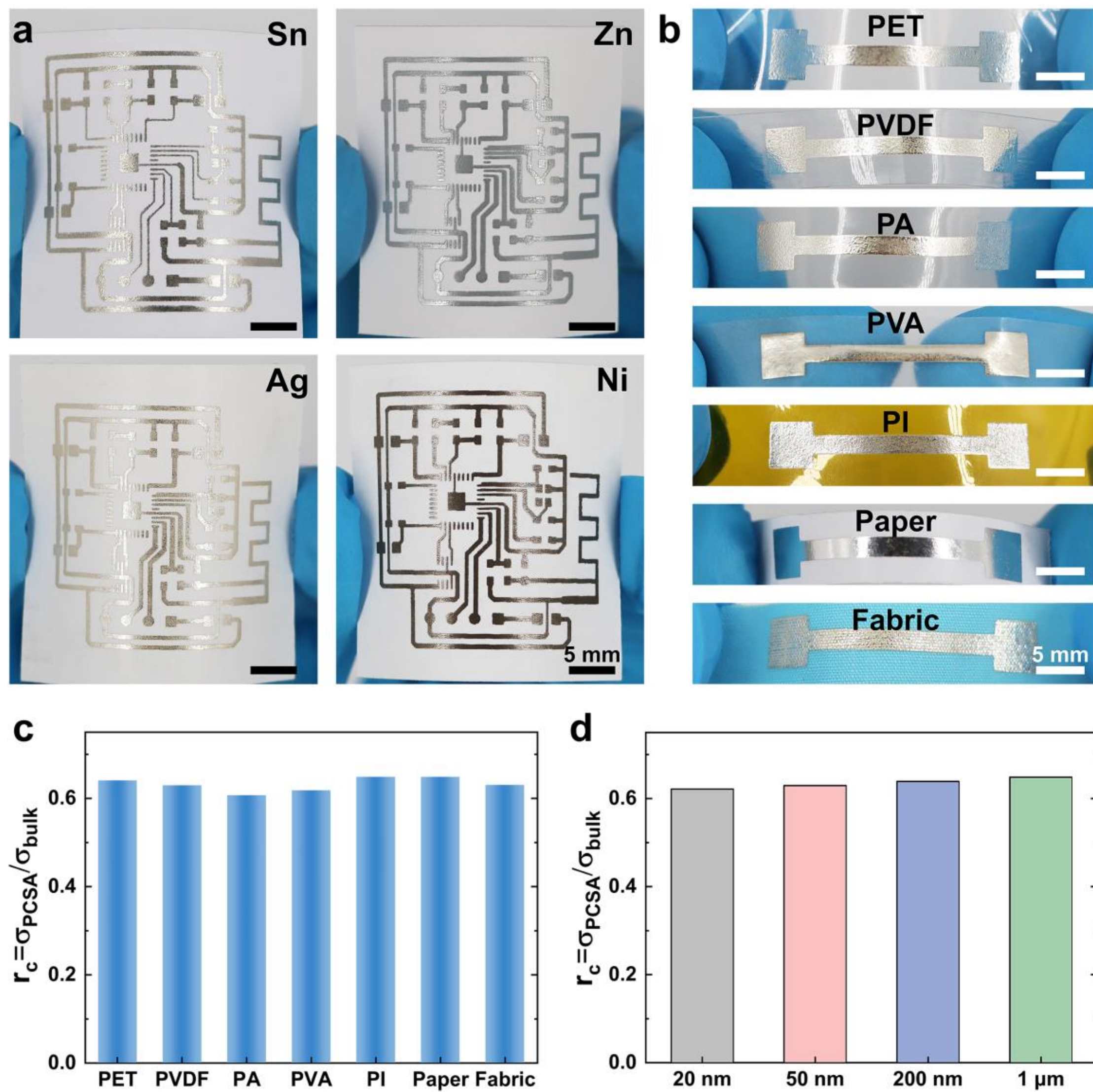

Fig.3| The PCSA for different-size metal particles on various flexible substrates. a, Photographs of Sn, Zn, Ag, and Ni-based circuits activated by the PCSA. **b**, Photographs of Ag-based printed electrodes (6 μm×2 mm×20 mm) with a dog-bone shape on the seven flexible substrates (PET-polyethylene glycol terephthalate, PVDF-polyvinylidene difluoride, PA-polyamide, PVA-Poly(vinyl alcohol), PI-polyimide). **c**, Electrical conductivity of the printed Ag electrodes on the seven flexible substrates activated by the PCSA (n = 3; independent samples). **d**, Electrical conductivity of the printed Ag electrodes with different particle sizes (n = 3; independent samples).

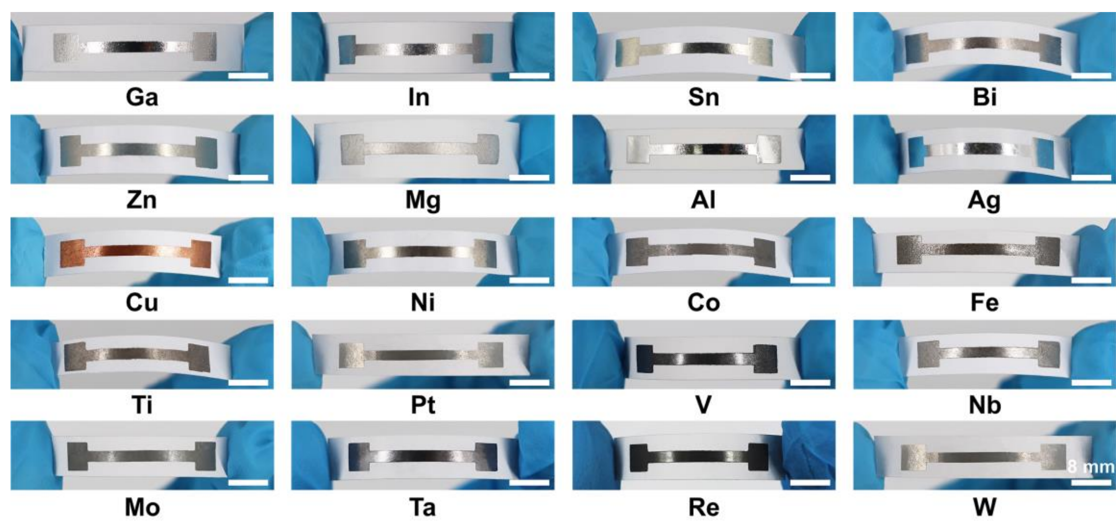

Fig.4| Photographs of the printed electrodes for 20 solid-metal particles activated by the PCSA method for the melting temperatures from room temperature (29.7 ºC for Ga) to 3422 ºC for W.

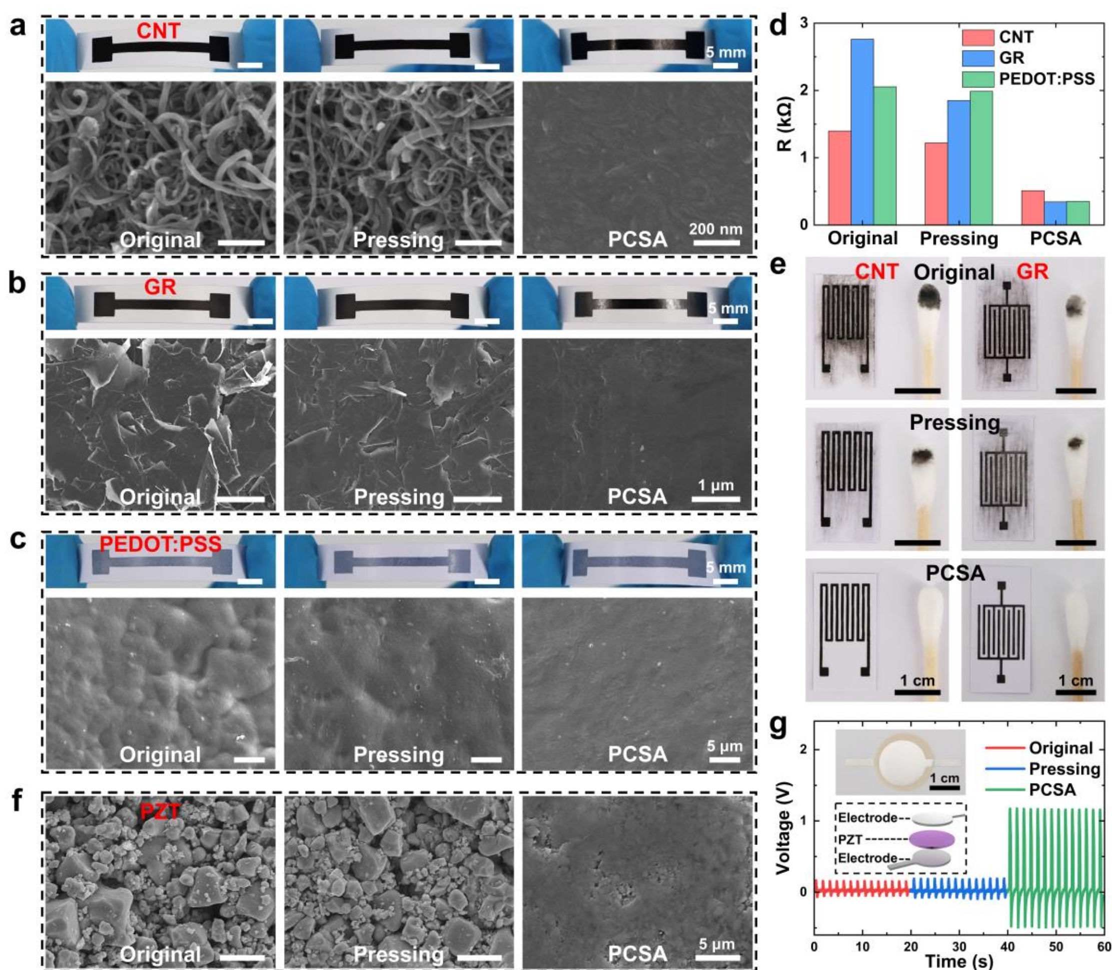

Fig.5| PCSA method for the printed nonmetal-particle pattern postprocessing. Photographs and SEM images of printed patterns under three states denoted by original (without posttreatment), pressing (10 MPa for 30 mins), and PCSA (0.3 MPa within 1 s) for **a**, CNT, **b**, GR, and **c,** PEDOT:PSS (n = 3; independent samples). **d**, The electrical conductivities of the CNT, GR, and PEDOT:PSS without/with posttreatment (n = 3; independent samples). **e**, Destructive testing of the printed patterns without/with posttreatment by wiping with a cotton swab. **f**, SEM images of printed PZT patterns without/with posttreatment (n = 3; independent samples). **g**, Impact of the posttreatment methods on the output voltage of printed PZT film under 20 kPa.

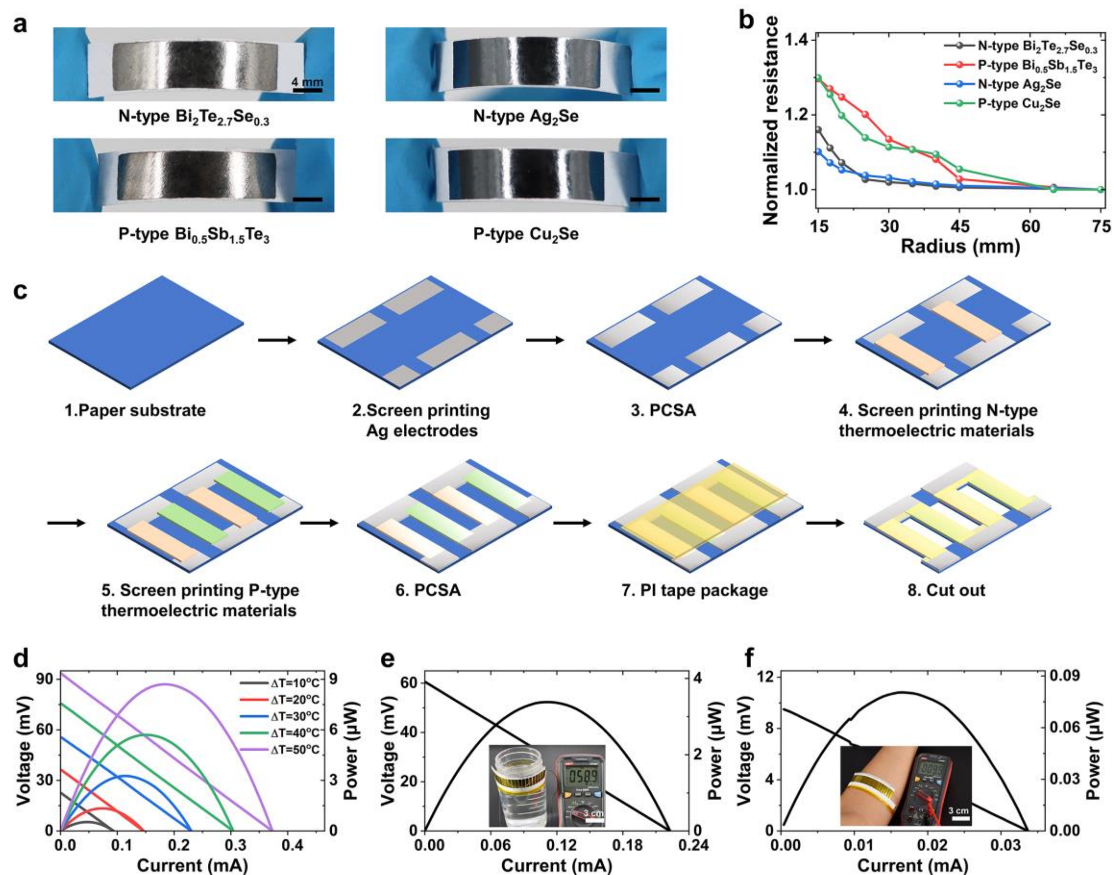

Fig.6| PCSA method for integratively fabricating FTEG. **a**, Photographs of the printed thermoelectric film activated by the PCSA method. **b**, Impacts of bending radius on the electrical conductivity of the printed thermoelectric film (12 μm × 4 mm × 20 mm) on a paper substrate. **c**, Schematic diagram of FTEG preparation process based on screen printing and PCSA methods. **d**, Current-voltage cukrves of FTEG with ten pairs of P/N-type ($Bi_2Te_{2.7}Se_{0.3}$/$Bi_{0.5}Sb_{1.5}Te_3$) legs under various constant temperature differences. **e** and **f**, Current-voltage curves of F-TEG for harvesting heat from a cup filled with hot water (60 ºC) and the human body, respectively.

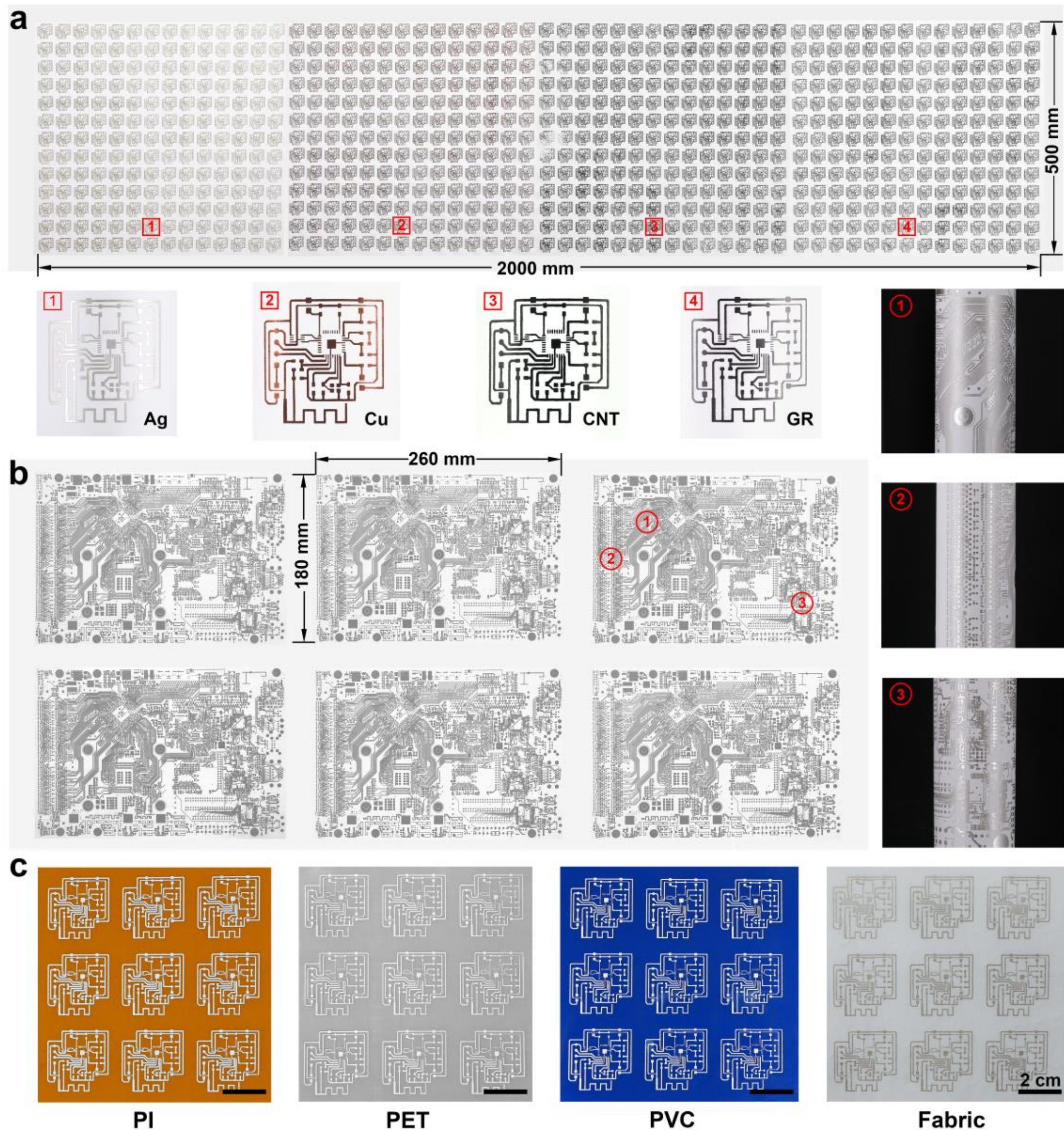

Fig.7| Roll-based PCSA for metal and nonmetal patterns on various flexible substrates. **a**, Photograph of activated Ag-, Cu-, CNT- and GR-based printed circuits. **b**, Photograph of activated Ag-based printed circuits with a large area. **c**, Photograph of the printed circuits on different flexible substrates.

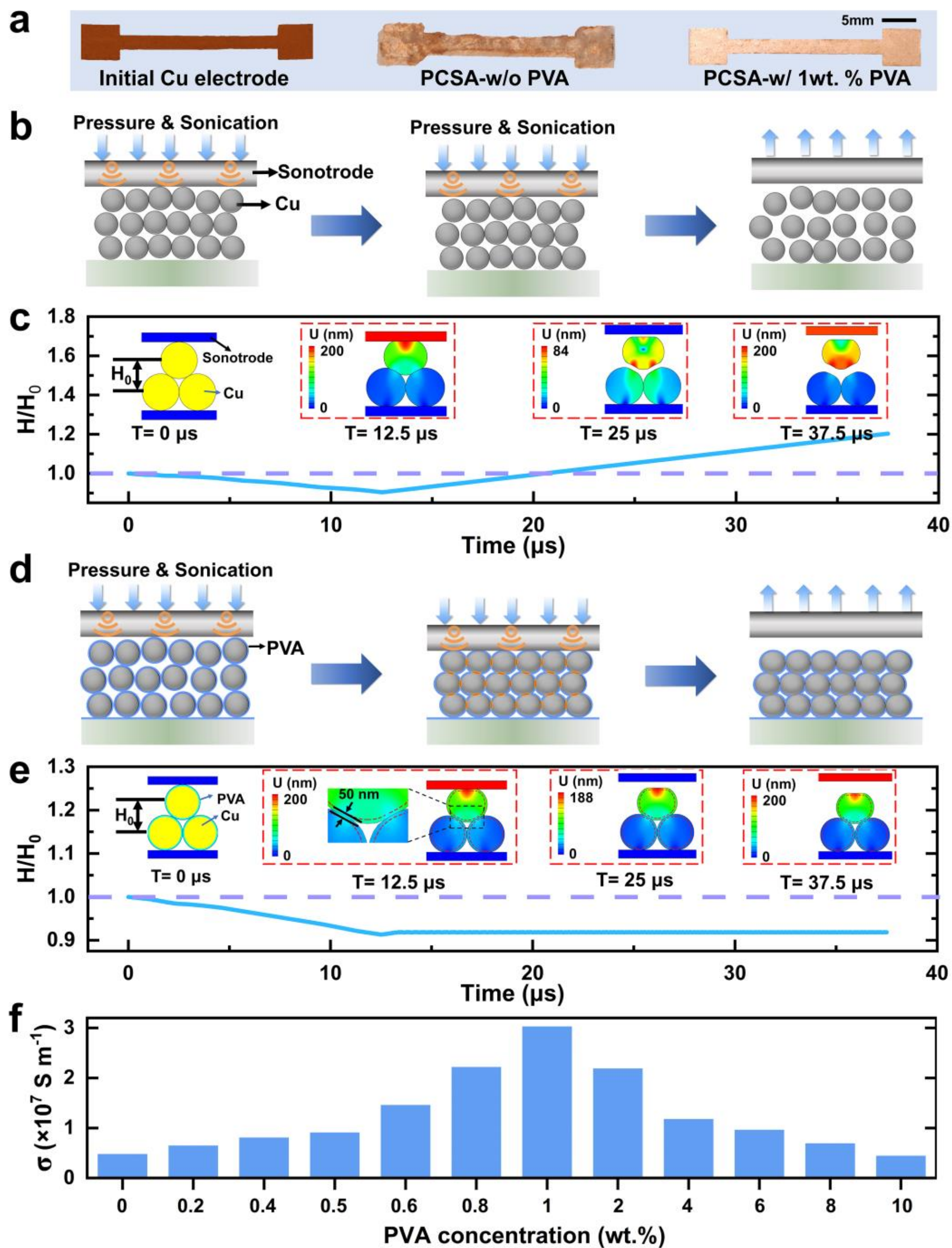

Fig.8| Suppressing particle segregation induced by sonication vibration. **a**, Photographs of the printed Cu nanoparticle-ink electrodes at the initial state (without activation), after activation by the PCSA without or with the coated PVA polymer. **b**, Illustration of particle segregation induced by sonication vibration. **c**, Simulation results of particle-particle elastic collision without interfacial adhesion inducing particle segregation. The distance between particles is denoted by H, and H_0 for the initial value (about 0.866 μm for the particle diameter of 1 μm); U is for the displacement. **d**, Illustration of particle adhered by the coated PVA for suppressing particle segregation induced by sonication vibration. **e**, Simulation results of particle-particle inelastic collision due to the coated polymer enhanced the energy dissipation at the particle interface. **f**, Impacts of the PVA concentration on the electrical conductivity of the printed circuits activated by the PCSA method (*n* = 3; independent samples). (Detailed discussion in Supplementary Note 2).

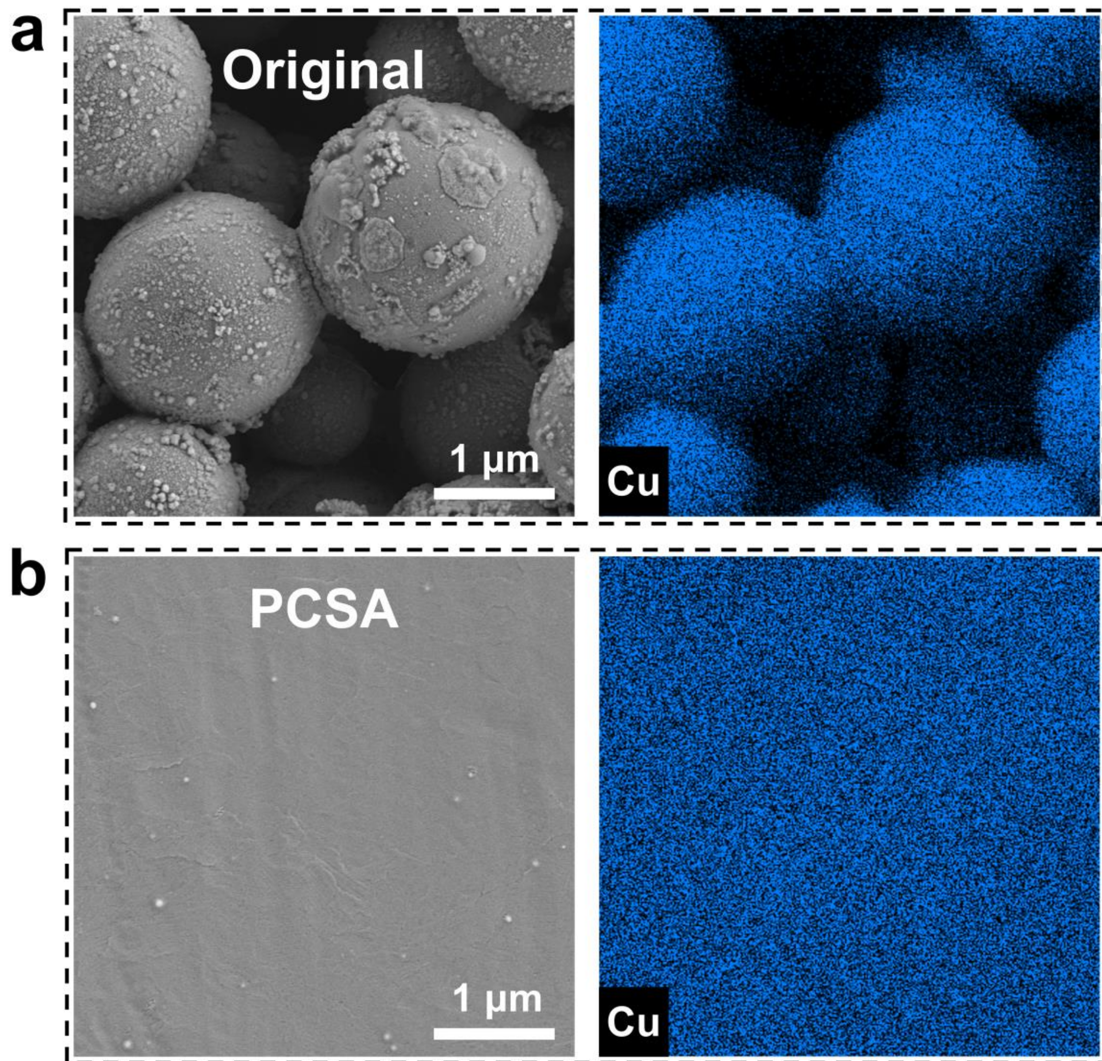

Fig.9| Microstructural and Cu distribution before/after the PCSA processing. SEM images and the corresponding EDS element mapping before (**a**) and after (**b**) after the PCSA processing, revealing the layers of surface oxidation and PVA polymer broken by the PCSA n = 4; independent samples).

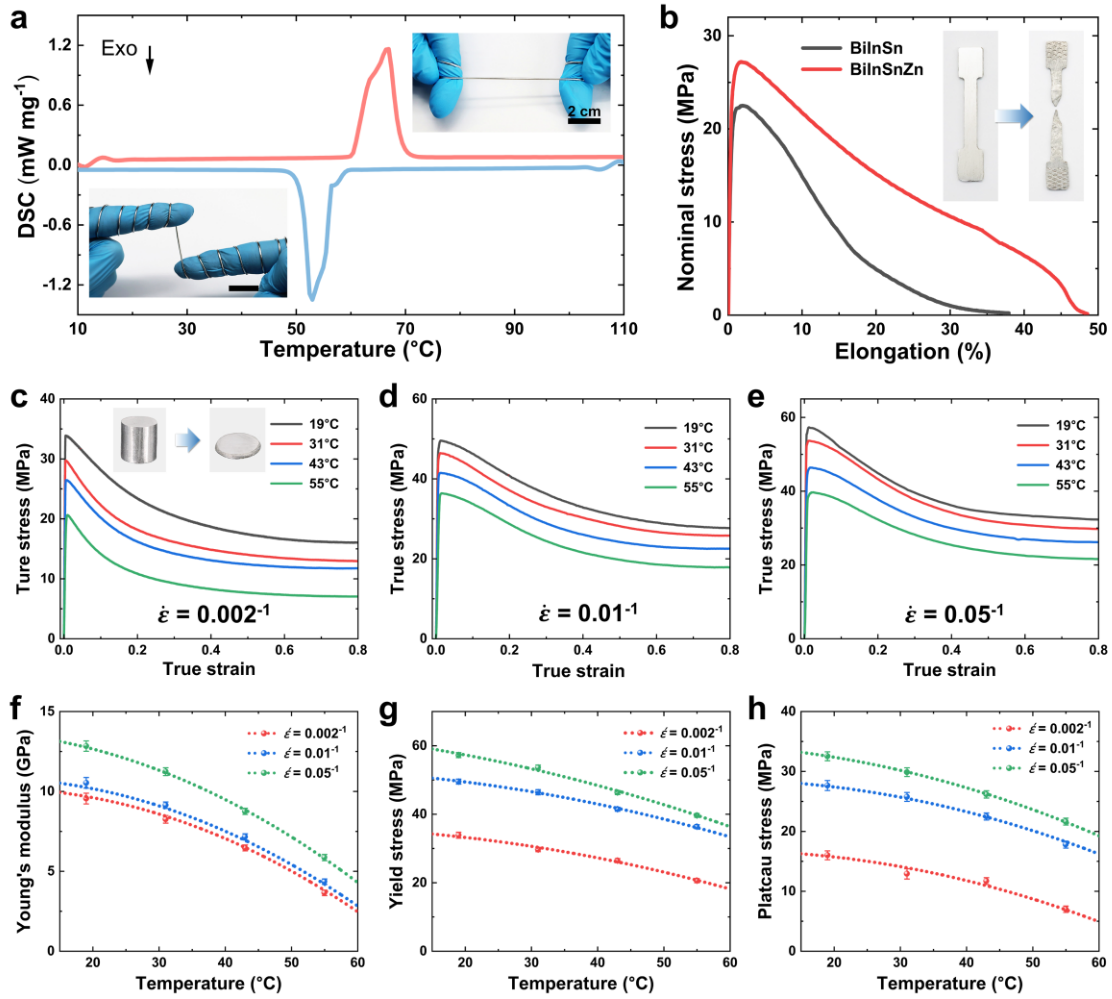

Fig.10| a, DSC curve of BiInSnZn. Photographs of BiInSnZn filled into the silicon tube (0.5mm in inner radius) under solid and liquid states, which is wrapped around the fingers. **b,** Ductility tests of BiInSnZn and BiInSn alloy, denoting its better ductility than BiInSn. **c, d,** and **e**, The strain-stress relations for BiInSnZn under different temperatures and strain rates. **f,** Elastic modulus, **g,** Yield Stress, and **h,** Plateau stress under different temperatures and strain rates.

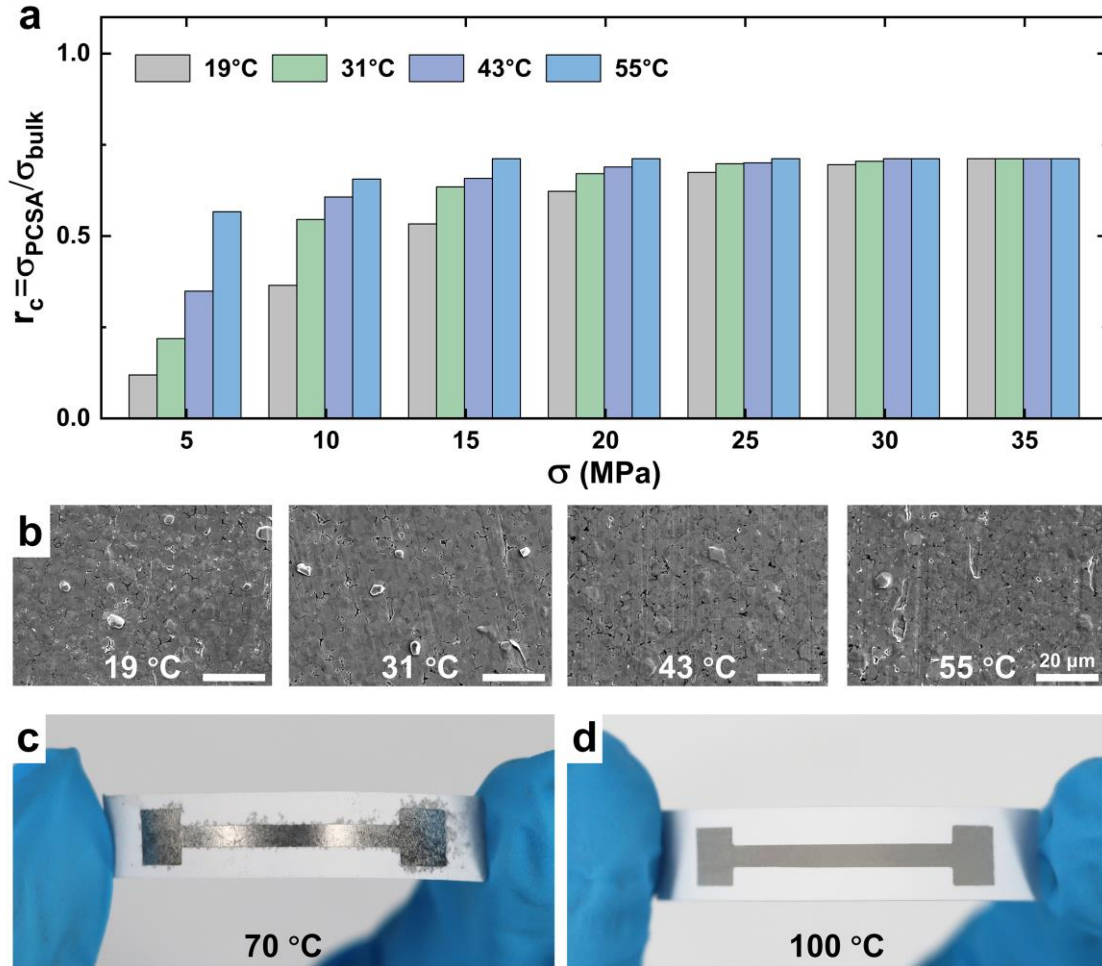

Fig.11| a, electrical conductivities of printed BiInSnZn electrode under different pressing and temperatures (n = 3; independent samples). **b,** SEM of surface structure for the printed BiInSnZn electrode through pressing with 35MPa at different temperatures (n = 3; independent samples). **c,** Photograph of the printed BiInSnZn electrode surface through pressing with 10 MPa at 70 ºC. It is observed that the electrode surface is damaged due to the large pressure applied to BiInSnZn in the liquid state. **d,** Photograph of the printed BiInSnZn electrode surface after thermal treatment at 100 ºC for 30 mins, which cannot activate the BiInSnZn particles bonding due to the particle gap, residual organics, and the oxide layer.

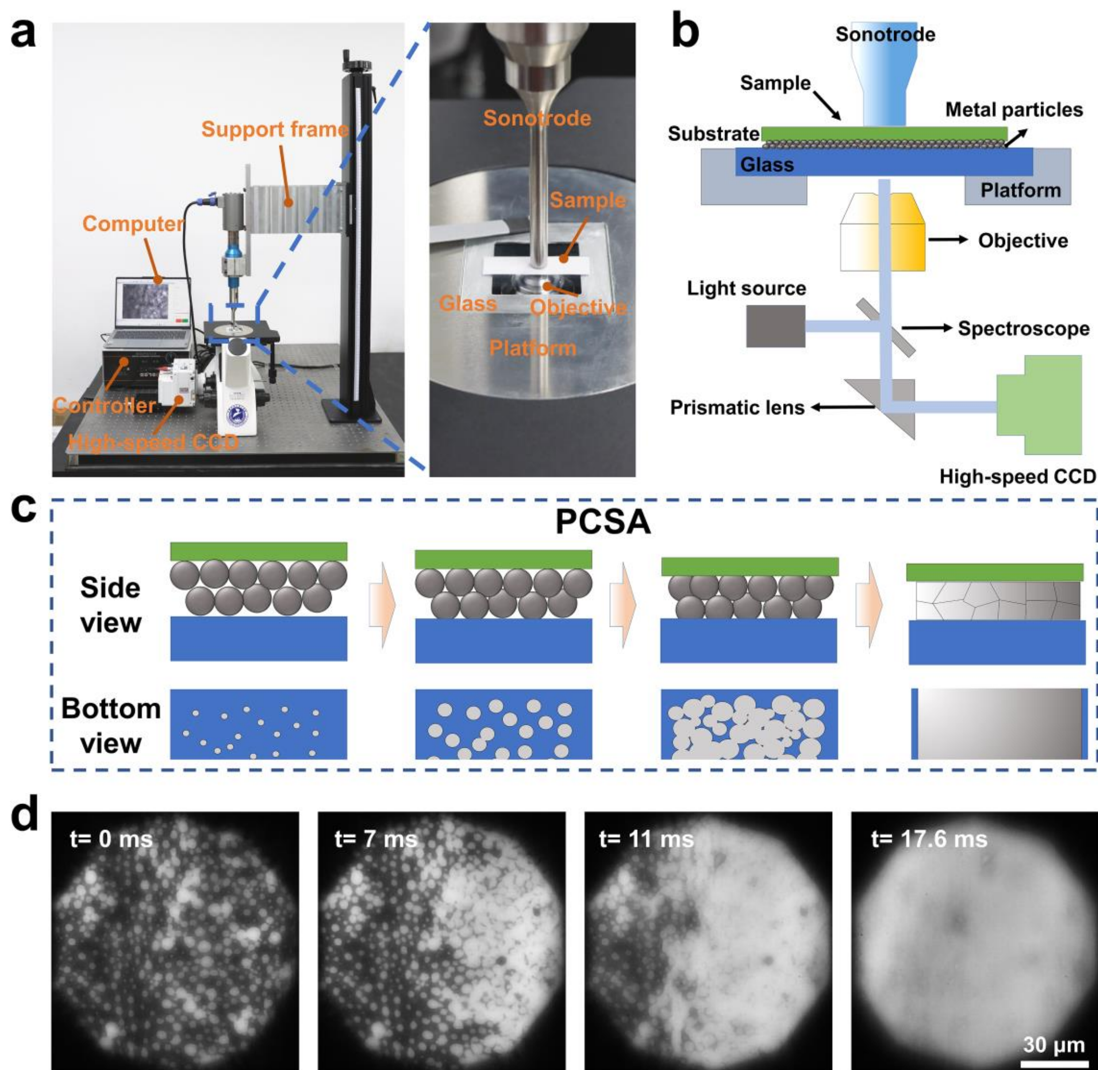

Fig. 12| Real-time observation of particle microstructure densification evolution during the PCSA process. **a**, Real-time observation platform composition, including sample loading platform, PCSA execution component, modified optical microscope, high-speed CCD and controller. **b**, Principle illustration of real-time observation. c, Illustration of observation view during the PCSA process. **d**, Optical images of BiInSnZn particle microstructure densification evolution during the PCSA process (corresponding to Case 3 in Supplementary Movie 6). The ultrasonic generator output energy is 180 W, the constrained pressure is 0.35 MPa and 22000 frames per second are for CCD (n = 4; independent experiments).

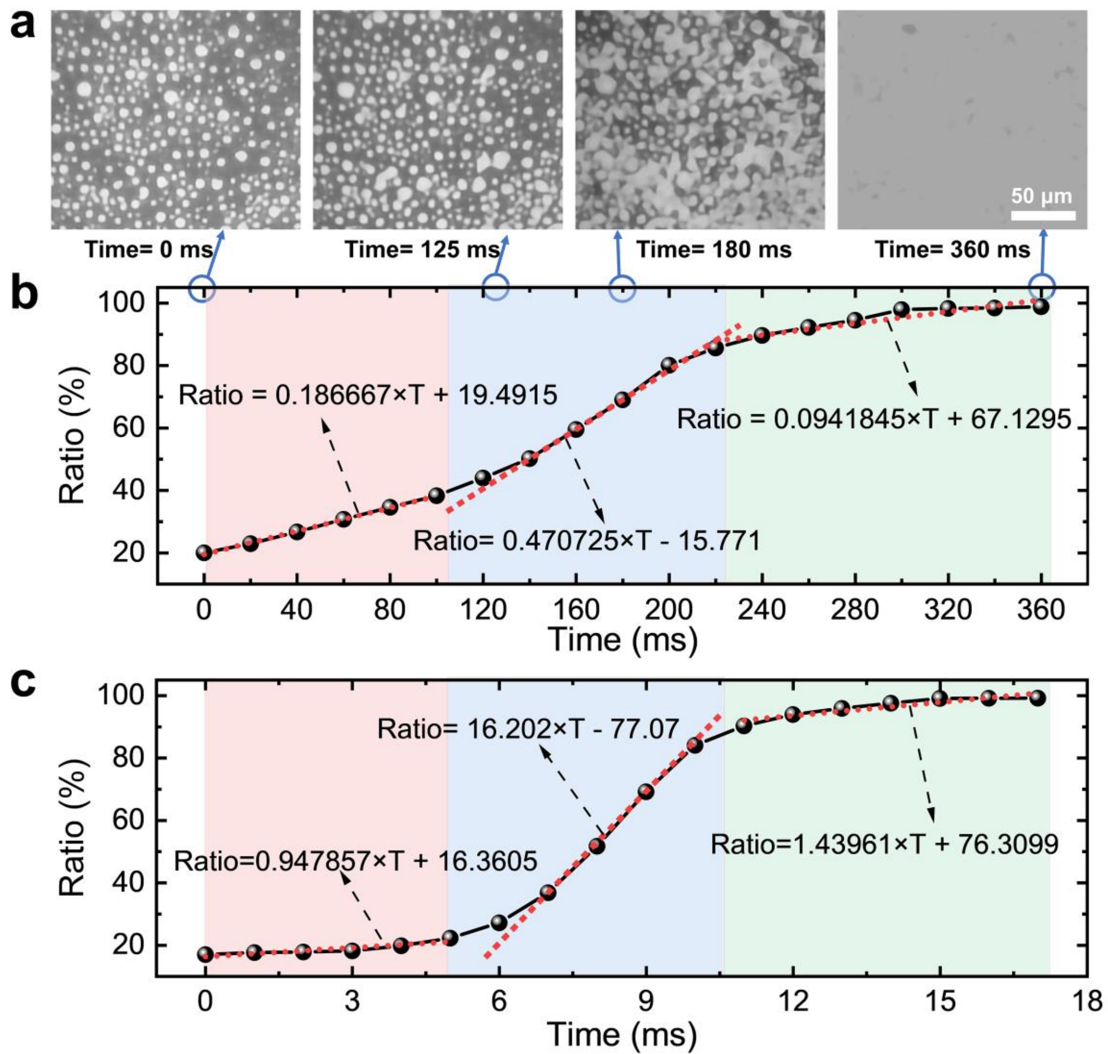

Fig. 13| Microstructure densification evolution during the PCSA process. a, Optical images of particle microstructure densification evolution during the PCSA process (corresponding to Case 1 in Supplementary Movie 6). The ultrasonic generator output energy is 80 W, the constrained pressure is 0.20 MPa and 10000 frames per second are for CCD ($n = 4$; independent experiments). **b**, Densification ratio per operation time. The densification ratio is defined as the particle area ratio on the glass substrate. **c**, Densification ratio per operation time (corresponding to Case 2 in Supplementary Movie 6) under a large ultrasonic generator output energy of 180 W and a constrained pressure of 0.35 MPa. 10000 frames per second are for CCD.

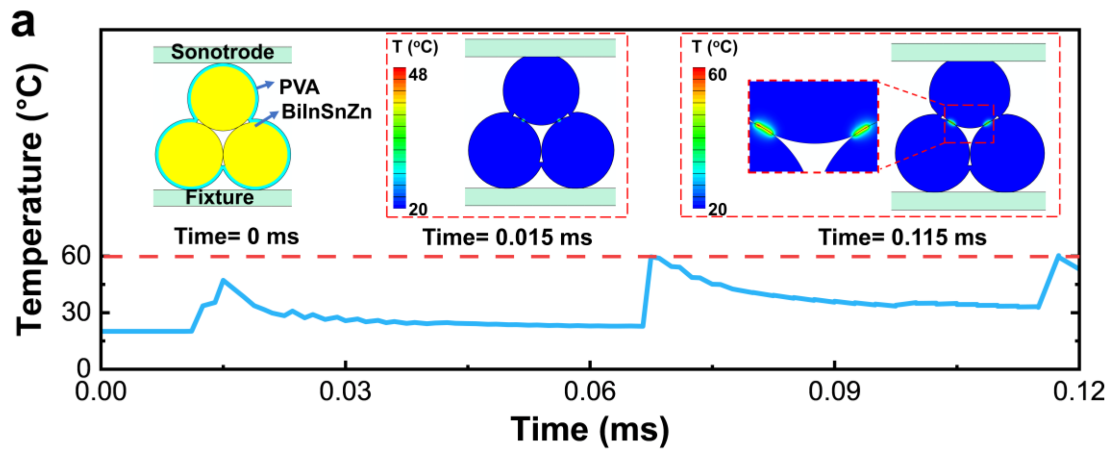

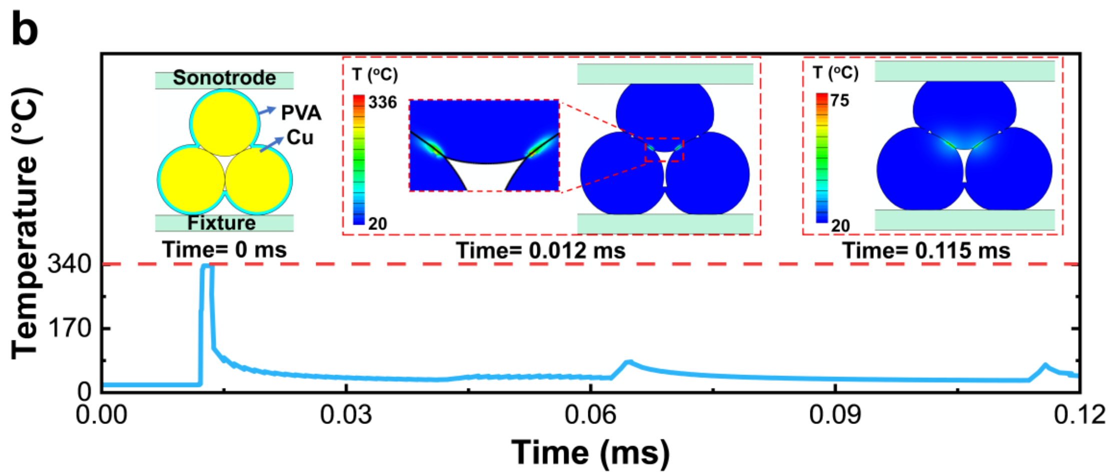

Fig.14| Simulation results of peak temperature induced by particle interface friction. **a**, Peak temperature at the BiInSnZn particle interface with an amplitude of 0.05 μm vibration within three vibration cycles. **b**, Peak temperature at the Cu particle interface with an amplitude of 0.3 μm within three vibration cycles (Detailed discussion in Supplementary Note 2).

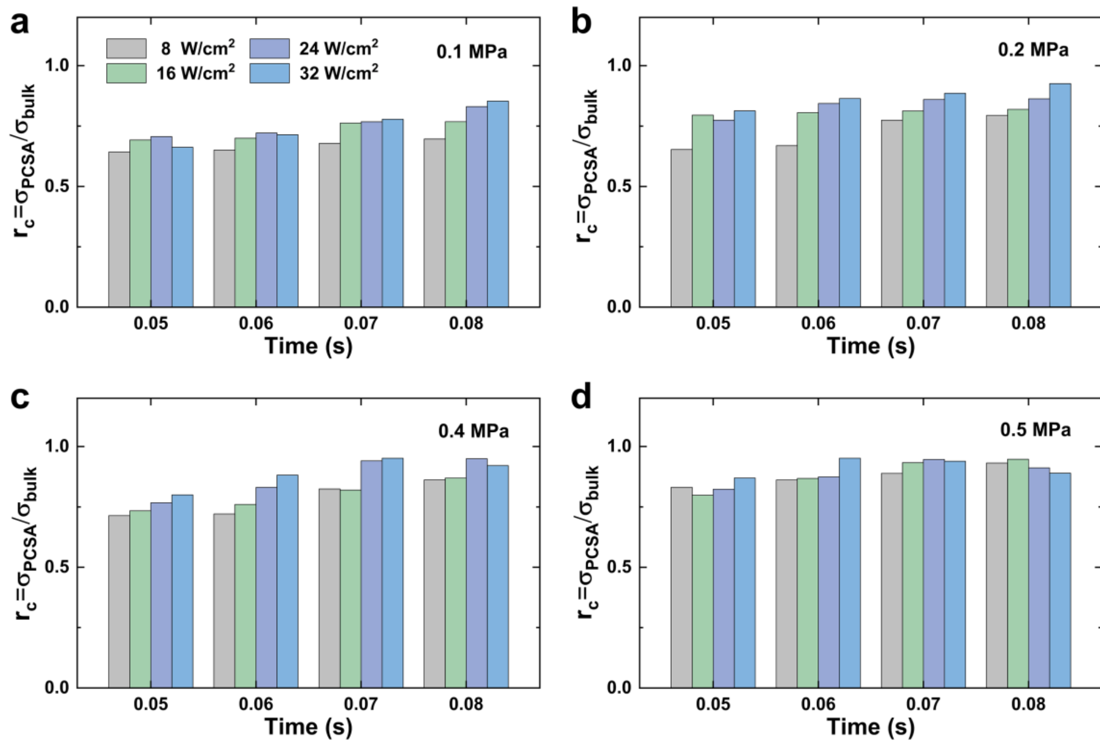

Fig.15| The conductivity of the printed BiInSnZn electrodes activated by PCSA under different operating parameters of constrained pressure, action time, and sonication power density ($n = 3$; independent samples).

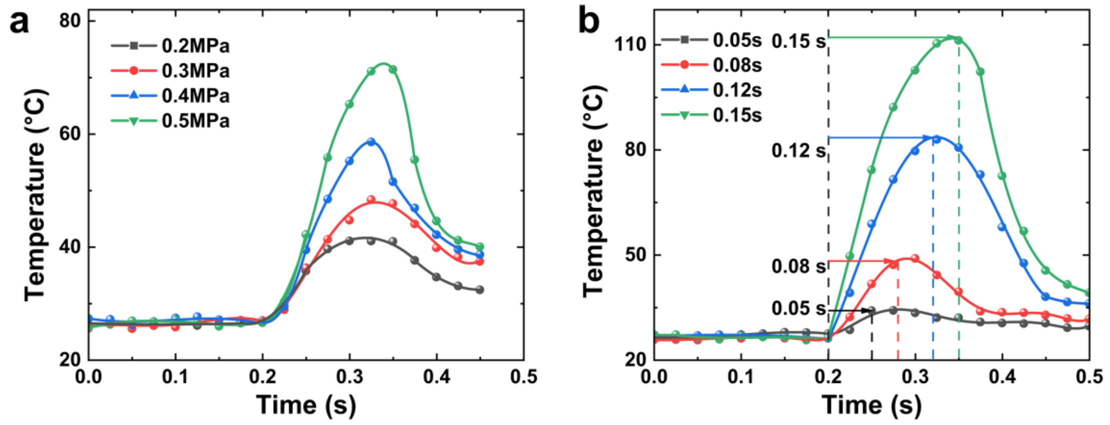

Fig.16| Apparent surface temperature for high-melting-point metal particle a, Apparent surface temperature rises of the printed Cu electrodes during the PCSA process under different constrained pressures with t_a=0.1 s and S_p=8 W/cm^2, and **b,** under different activation times with P_s=0.5 MPa and S_p =8 W/cm^2.

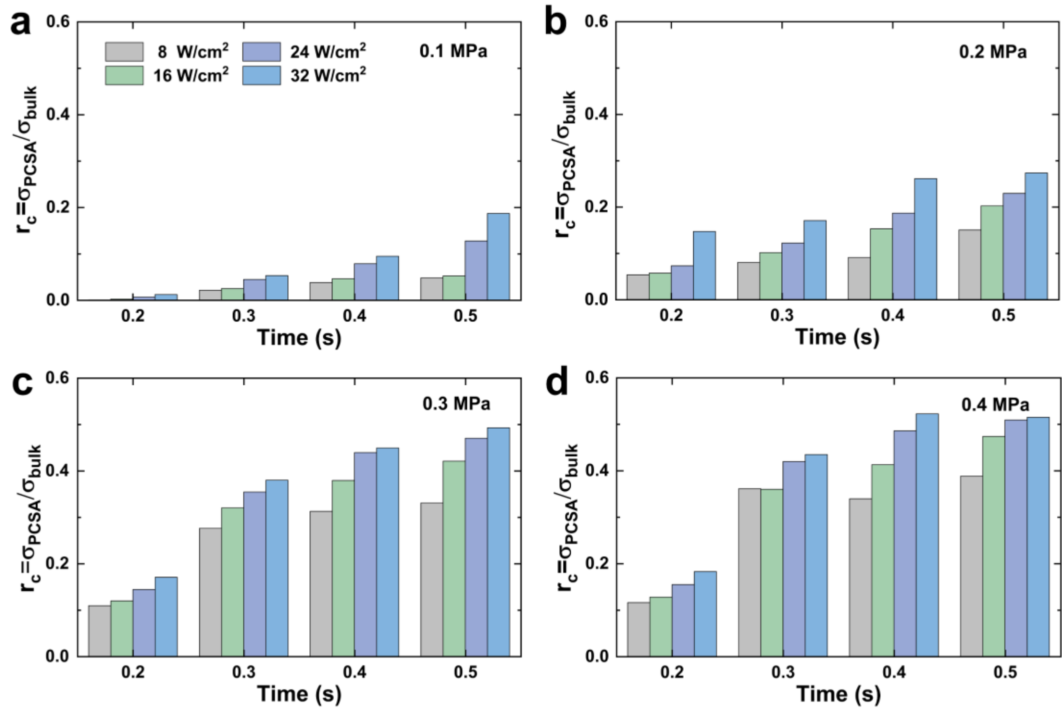

Fig.17| The conductivity of the printed Cu-particle electrodes activated by PCSA under different operating parameters of constrained pressure, action time, and sonication power density (n = 3; independent samples).

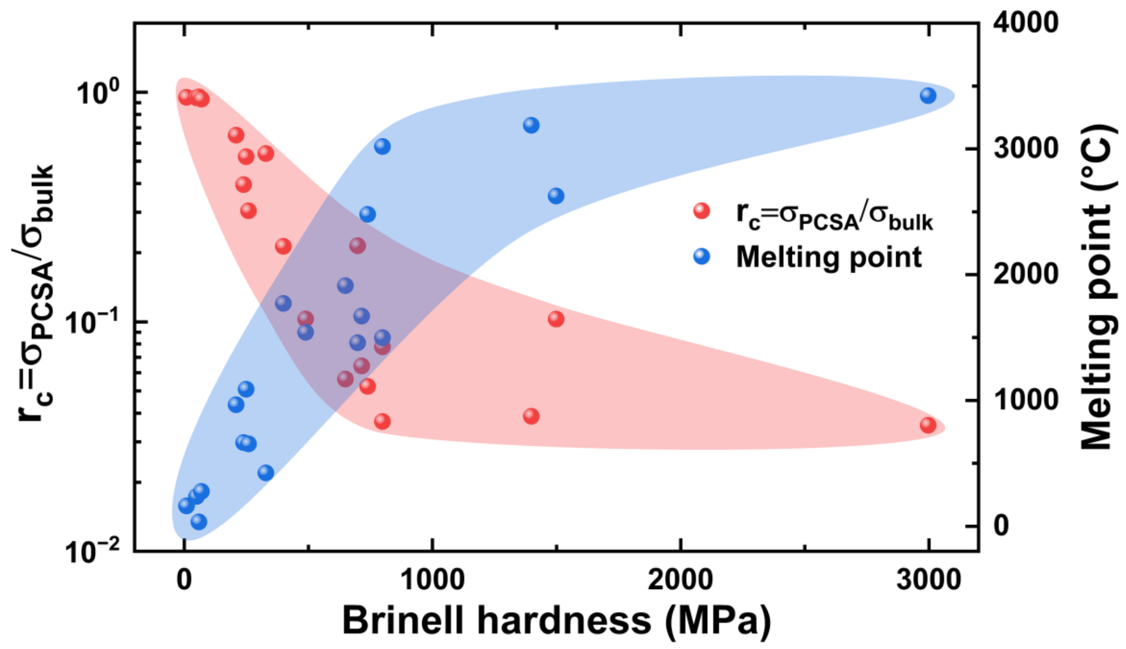

Fig.18| Impacts of the metal particle hardness on the activation performance of the PCSA method.

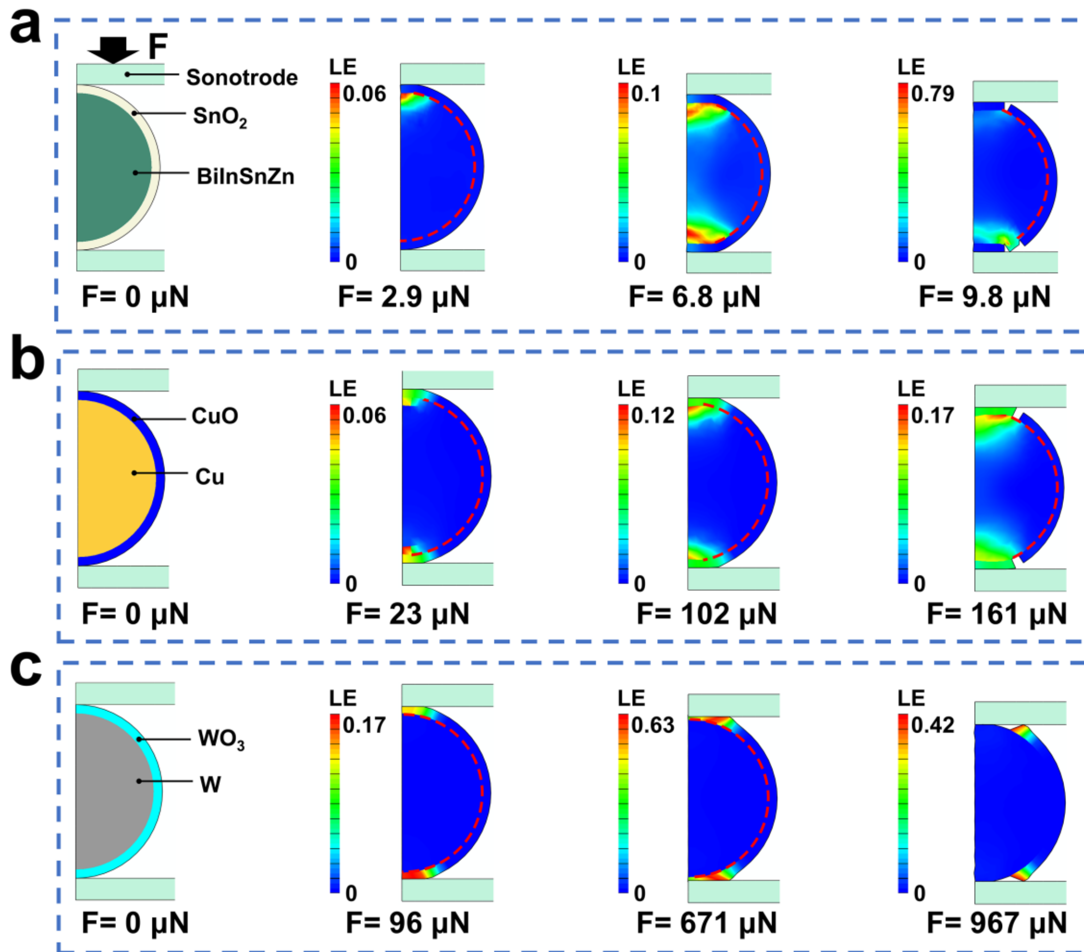

Fig.19| Impacts of the mechanical properties on the particle deformation. a, BiInSnZn (Young's Modulus: 12 GPa, T_m=60 ºC). **b**, Cu (Young's Modulus: 110 GPa, T_m=1084.8 ºC). **c**, W (Young's Modulus: 411 GPa, T_m=3422 ºC). (Detailed discussion in Supplementary Note 2).

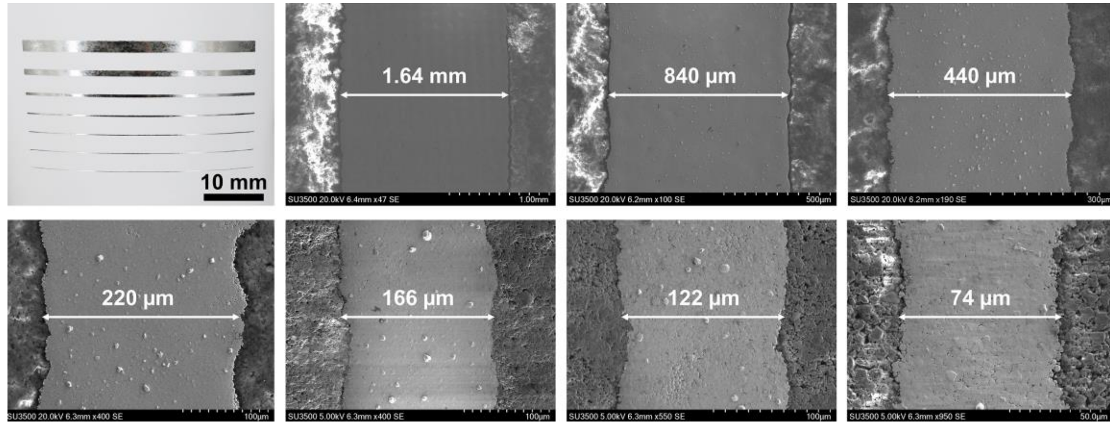

Fig.20| Photographs and SEMs of the printed BiInSnZn electrodes with different electrode widths activated by the PCSA method (n = 3; independent experiments).

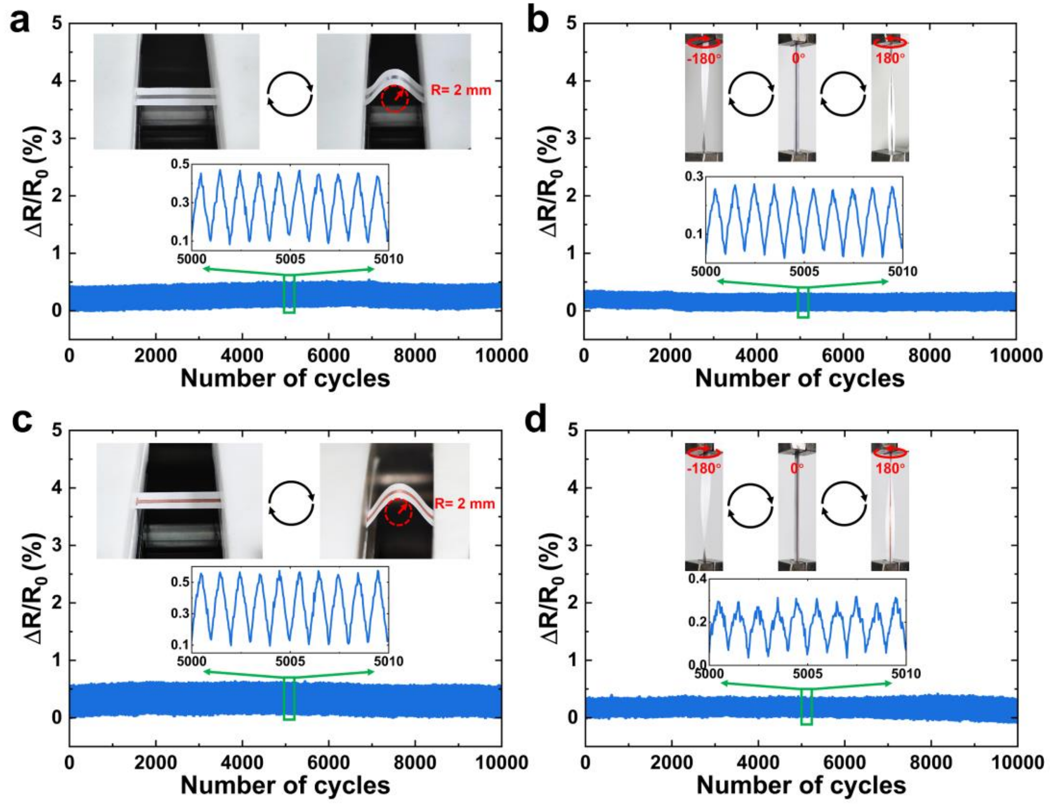

Fig.21| Resistance change of the printed BiInSnZn electrode under the conditions of **a**, the bending (with a radius of 2mm), and **b**, the twisting. The same tests are conducted for the printed Cu electrodes, as shown in **c** and **d**.

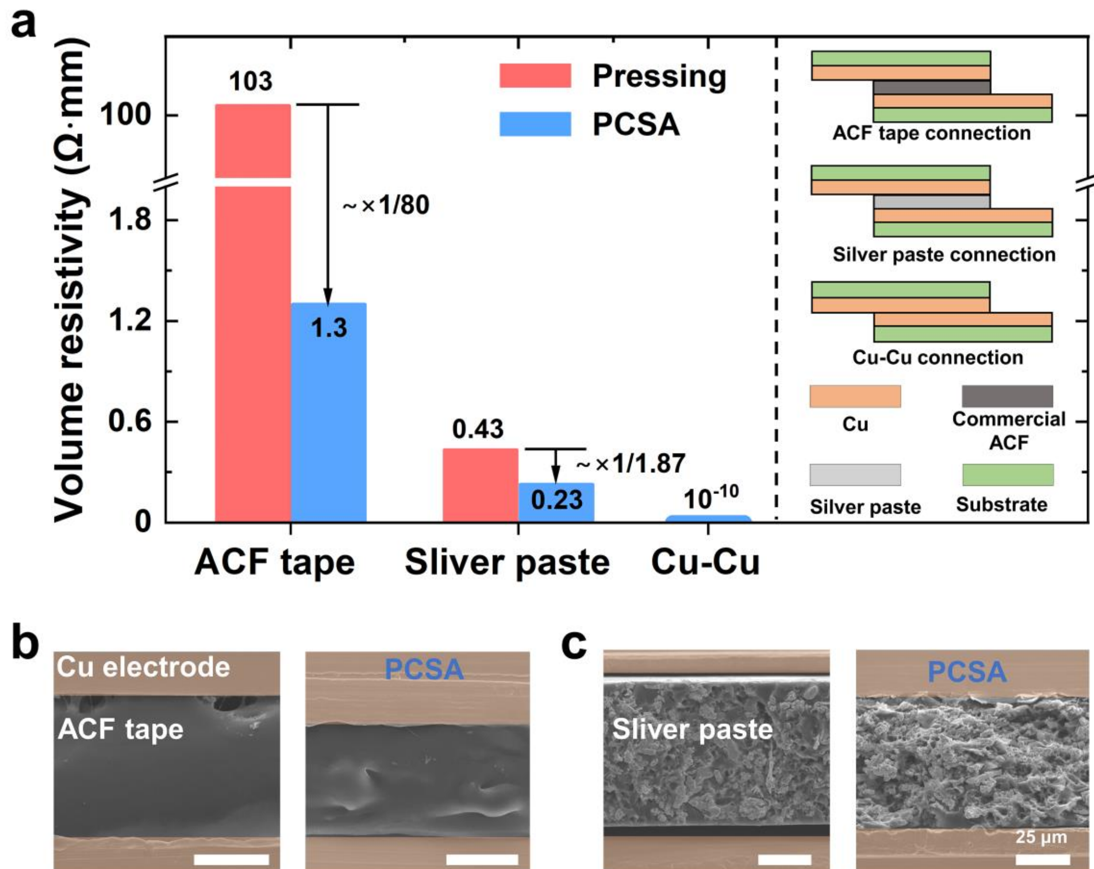

Fig.22| PCSA method for interconnection of the Cu electrodes. **a,** Volume resistivities between two Cu electrodes with interconnection layer of ACF tap or sliver paste after posttreatment methods of pressing (20 MPa for 30 min) and PCSA (0.3 MPa within 1 s), as well as non-paste by PCSA (n = 3; independent samples). **b,** SEMs of the interconnection layer of ACF tap after posttreatment of the pressing method and PCSA (n = 3; independent samples). **c,** SEM images of the interconnection layer of sliver paste after posttreatment of the pressing method and PCSA (n = 3; independent samples).

The ACF tape was cut into 5 mm×5 mm size by laser cutting and connected to two 5 mm wide and 2 cm long copper foils. The silver paste was printed on the 5mm × 5mm area of the copper foil, and another copper foil of the same size was connected. The volume resistivity is estimated by $\rho = RA/L$, where R is the connection resistance, A is the connection area, and L is the thickness of the electrical conductivity.

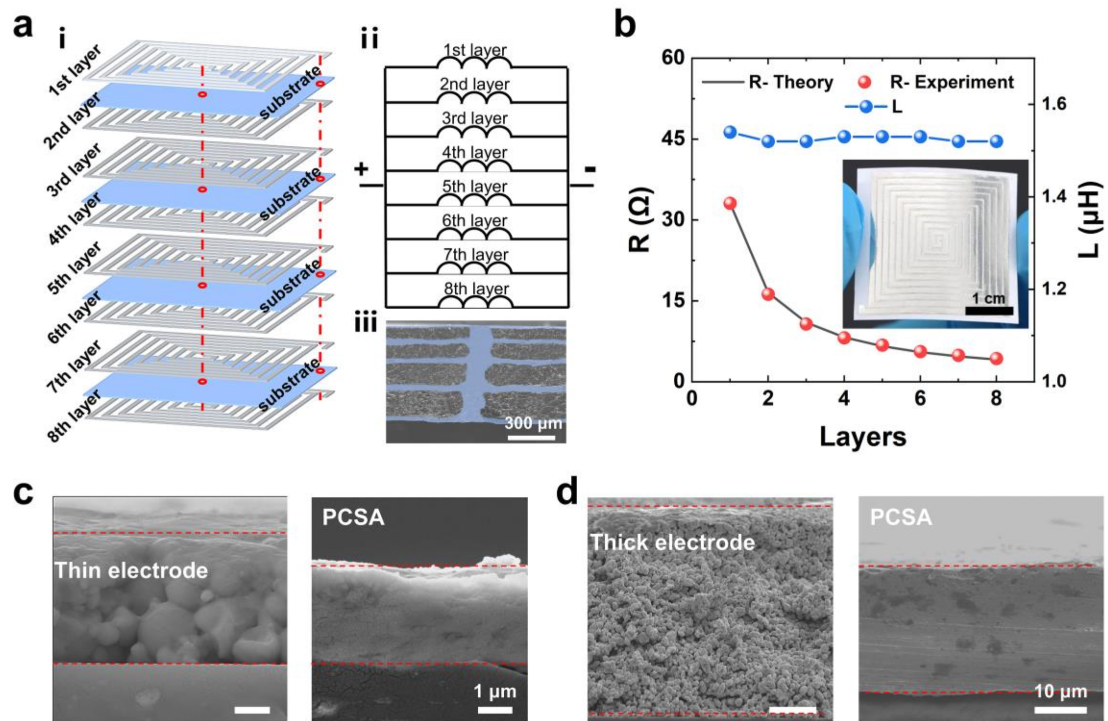

Fig.23| PCSA method for interconnection of multilayer circuits. **a**, Interconnection illustration of multilayer inductance coil and its microstructure from SEM. **b,** Inductance and resistance of the multilayer coil. **c,** SEM images of the printed thin electrode before/after the PCSA process (n = 3; independent samples). **d**, SEM images of the printed thick electrode before/after the PCSA process (n = 3; independent samples).

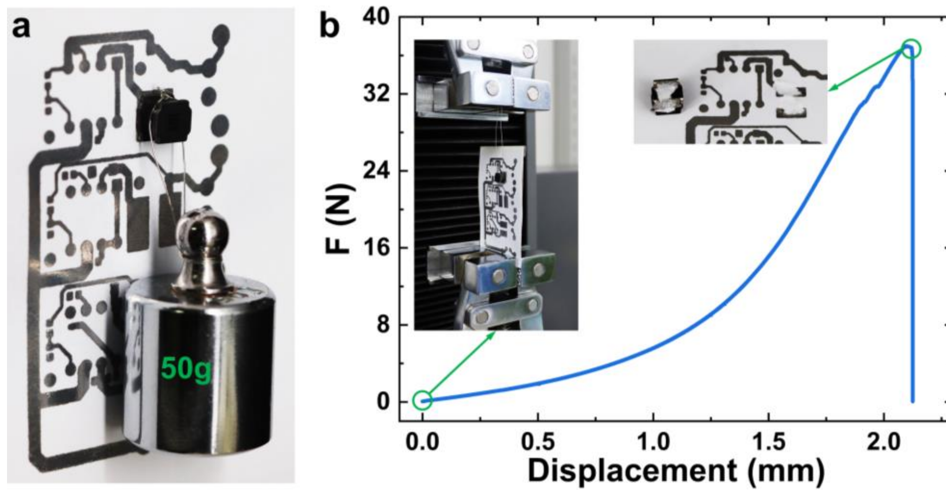

Fig.24| Adhesion force test a, Th electronic device strongly bonds with the printed BiInSnZn electrode activated by PCSA. **b**, Adhesion force testing of bonded electronic devices with printed electrodes. Contact separation does not occur between the electrode and the electronic device.

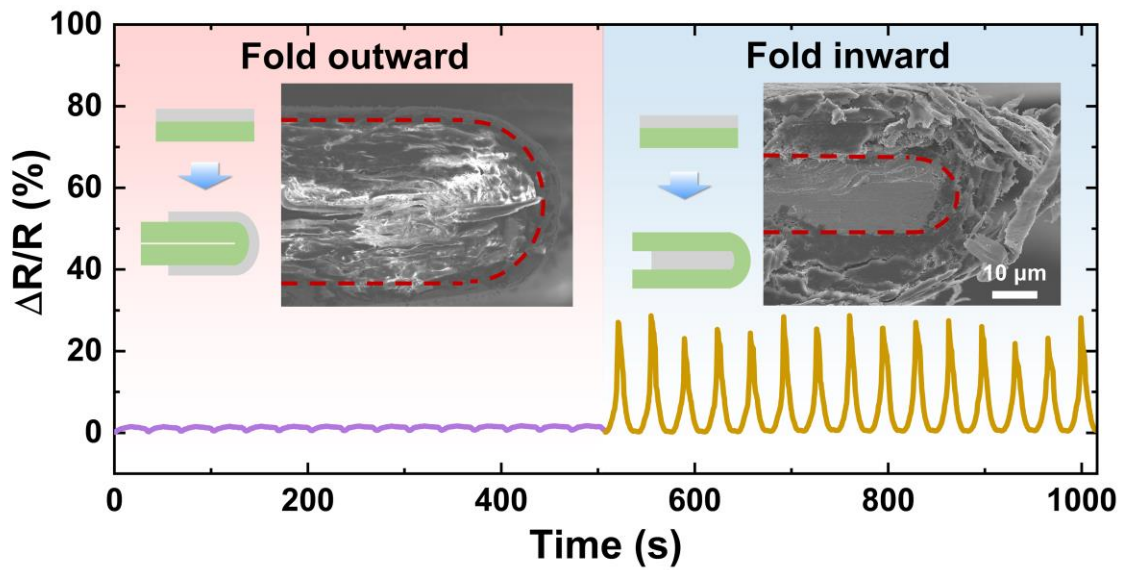

Fig.25| Resistance change of the printed BiInSnZn electrode under full-outward and full-inward folding. For the full-outward folding, the SEM shows a bending radius of 77 μm (n = 3; independent samples).

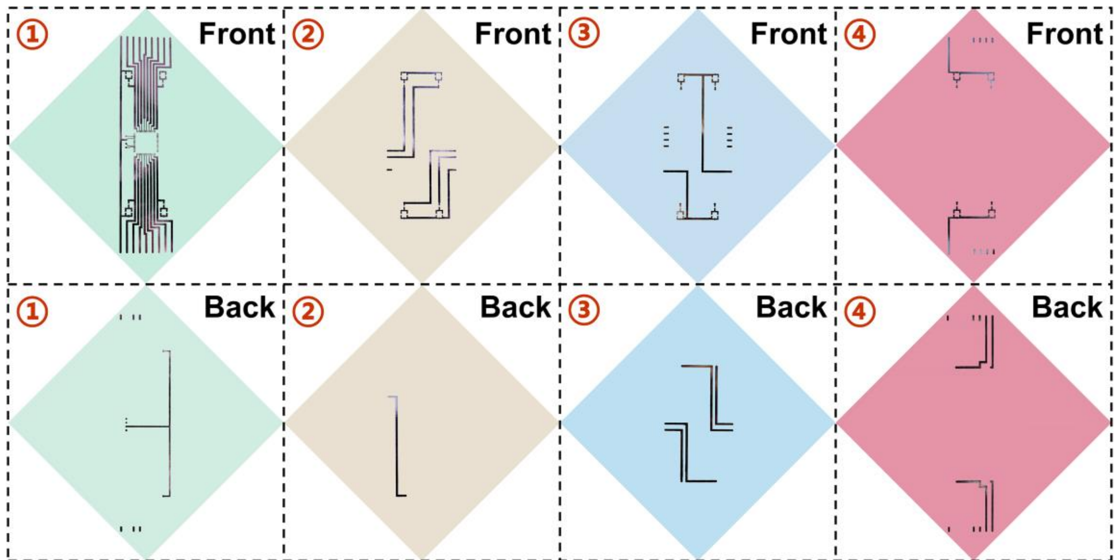

Fig.26| Photographs of the four foldable double-sided flexible circuits on paper substrates.

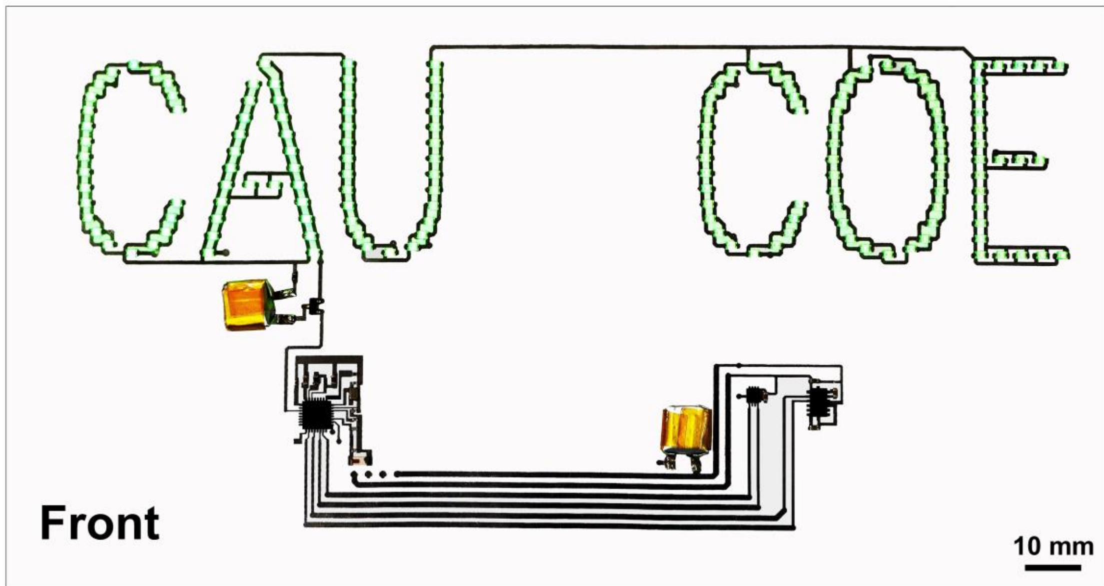

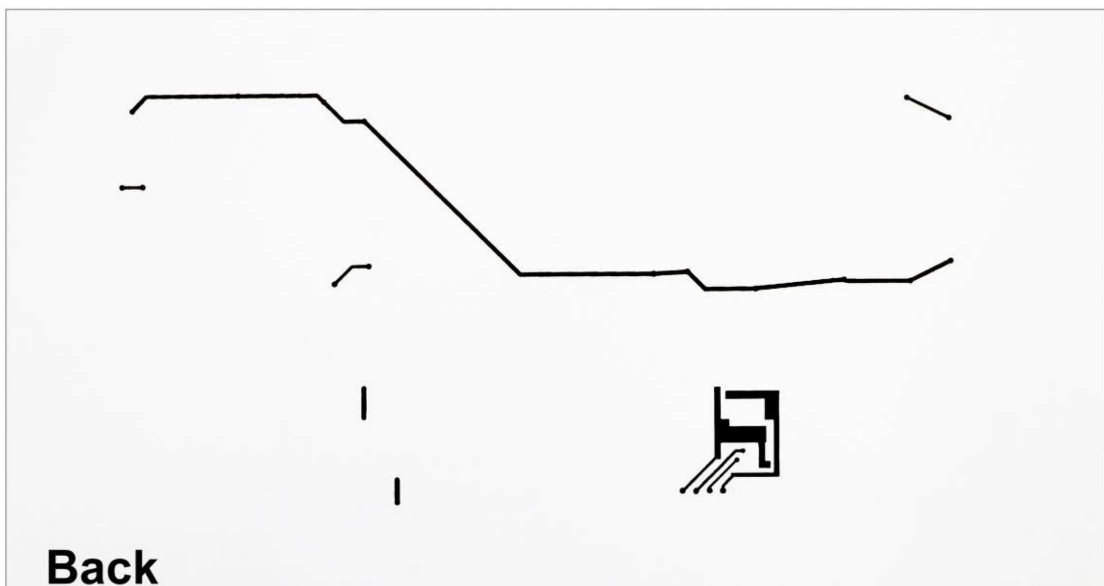

Fig.27| Photographs of the paper plane integrated with double-sided circuits and multiple electronic modules.

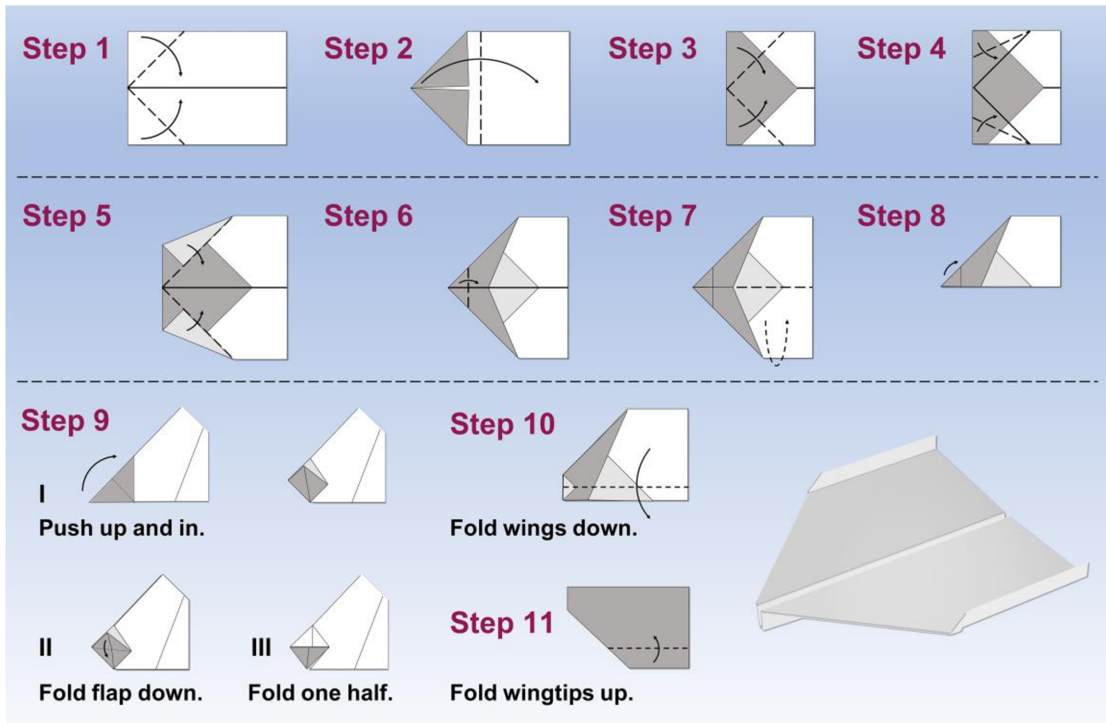

Fig.28| Illustration of the folding steps of the paper plane.

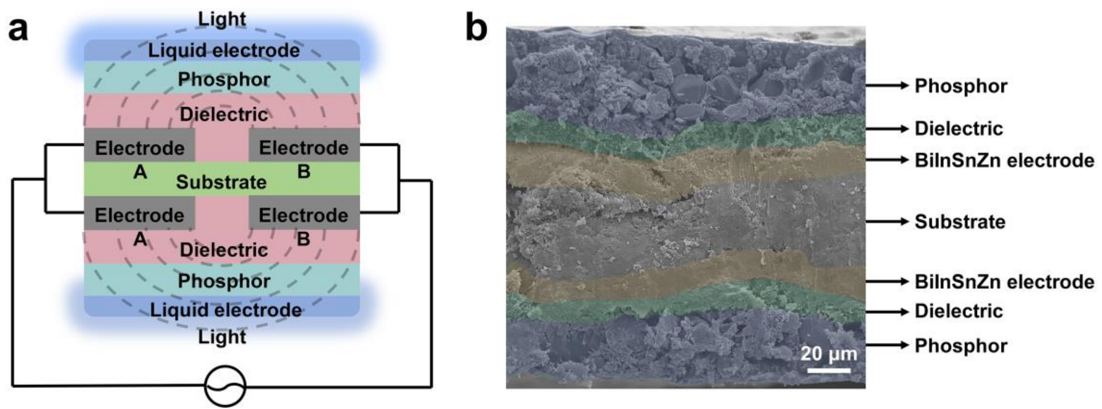

Fig.29| a, Illustration of the working principle of double-sided electroluminescent. **b,** SEM of the cross-section with different layers (n = 4; independent samples).

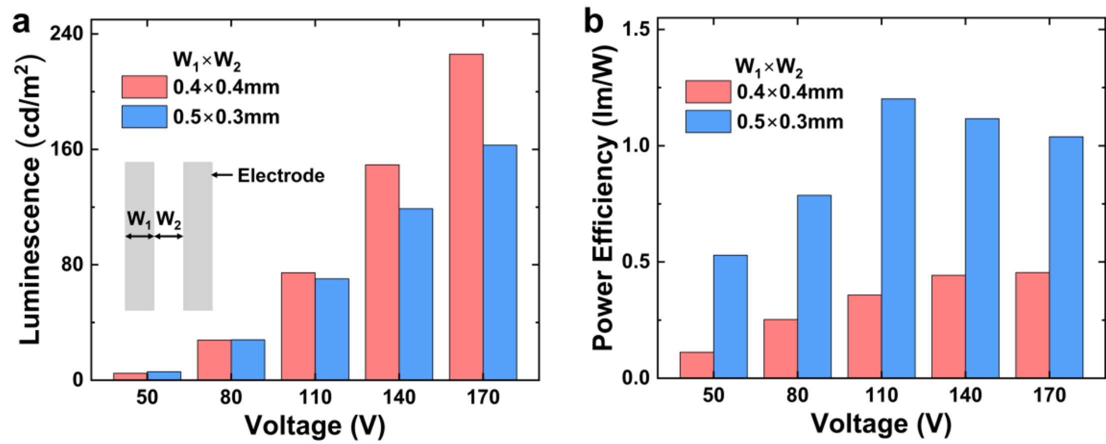

Fig.30| Impacts of the electrode width and spacing on (**a**) the luminescence and (**b**) power efficiency ($n = 4$; independent samples).

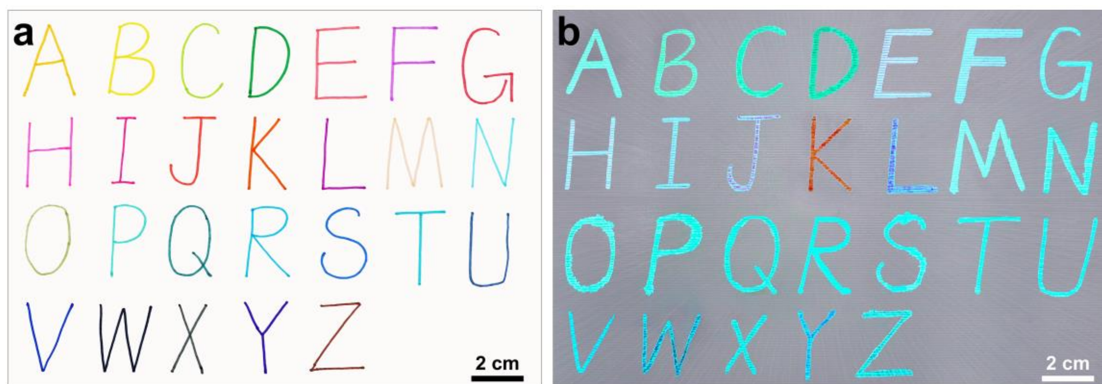

Fig.31| Photographs of writing colors with 26 watercolor pens **(a)** and **(b)** the corresponding luminescence colors.

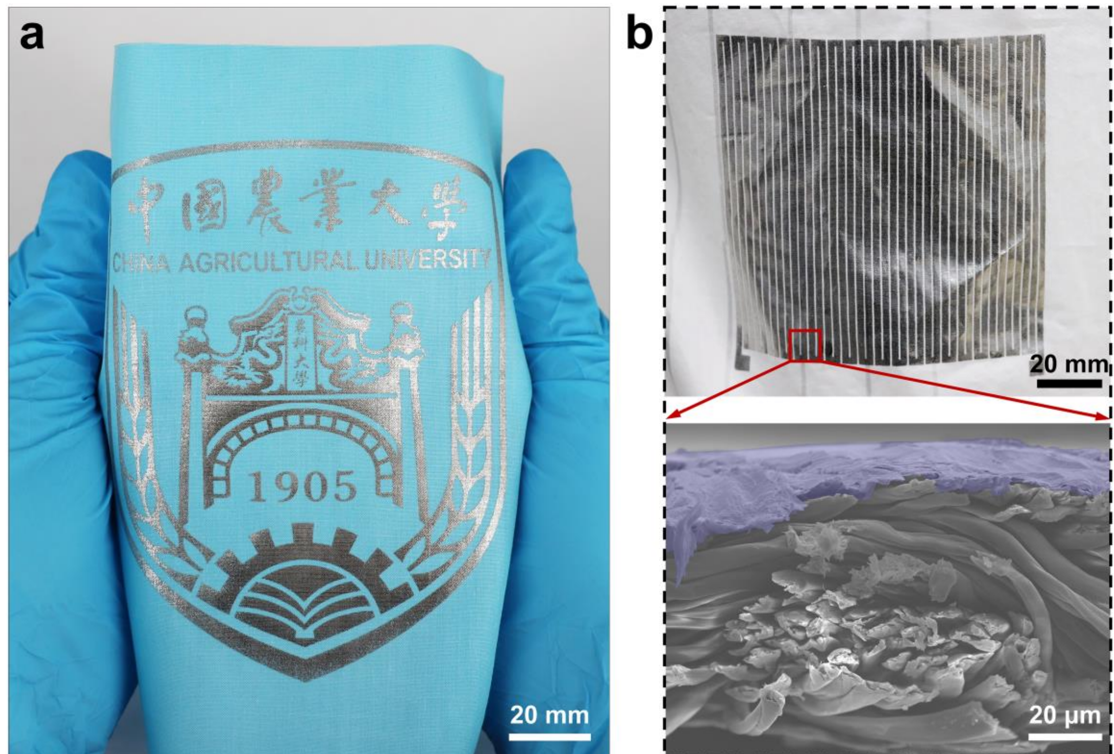

Fig.32| The printed patterns on fabric activated by the PCSA method. a, complicated patterns. **b,** Photograph and SEM image of the heating electrode on fabric (n = 3; independent samples).

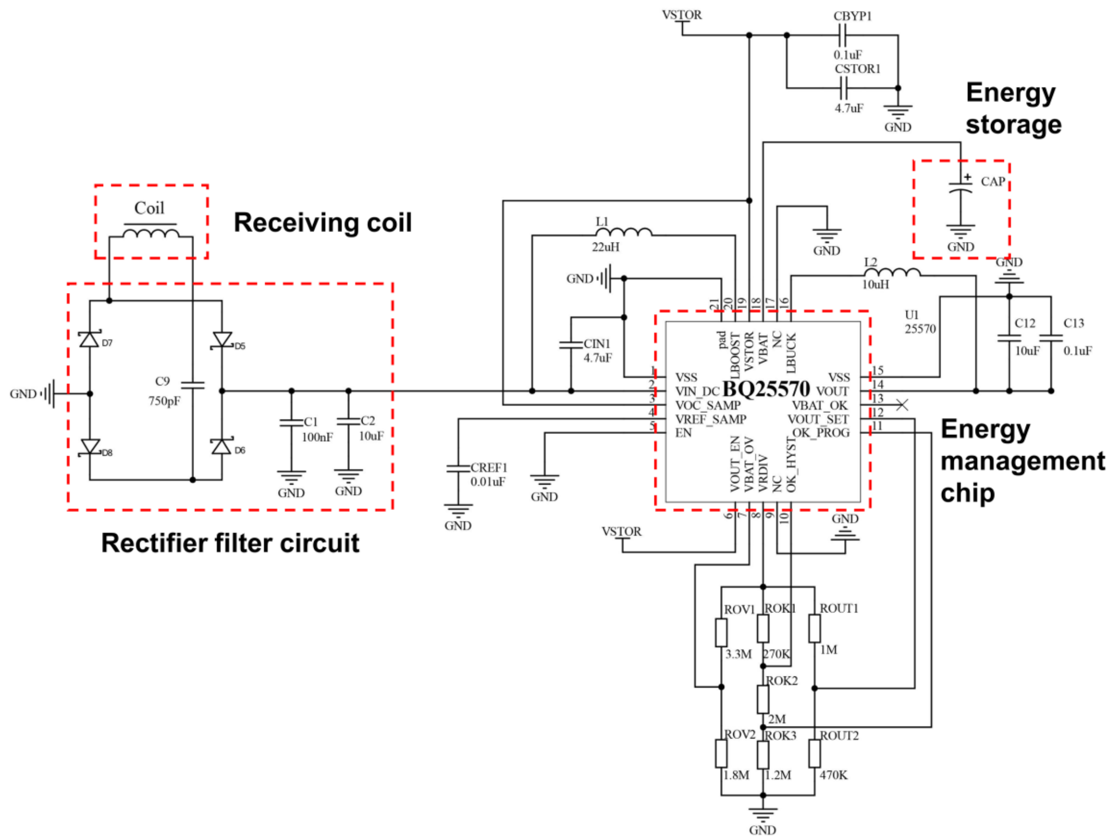

Fig.33| The wireless charging circuit, consisting of a receiver coil, AC-DC conversion circuit integrated with electronic components, and supercapacitor energy storage module.

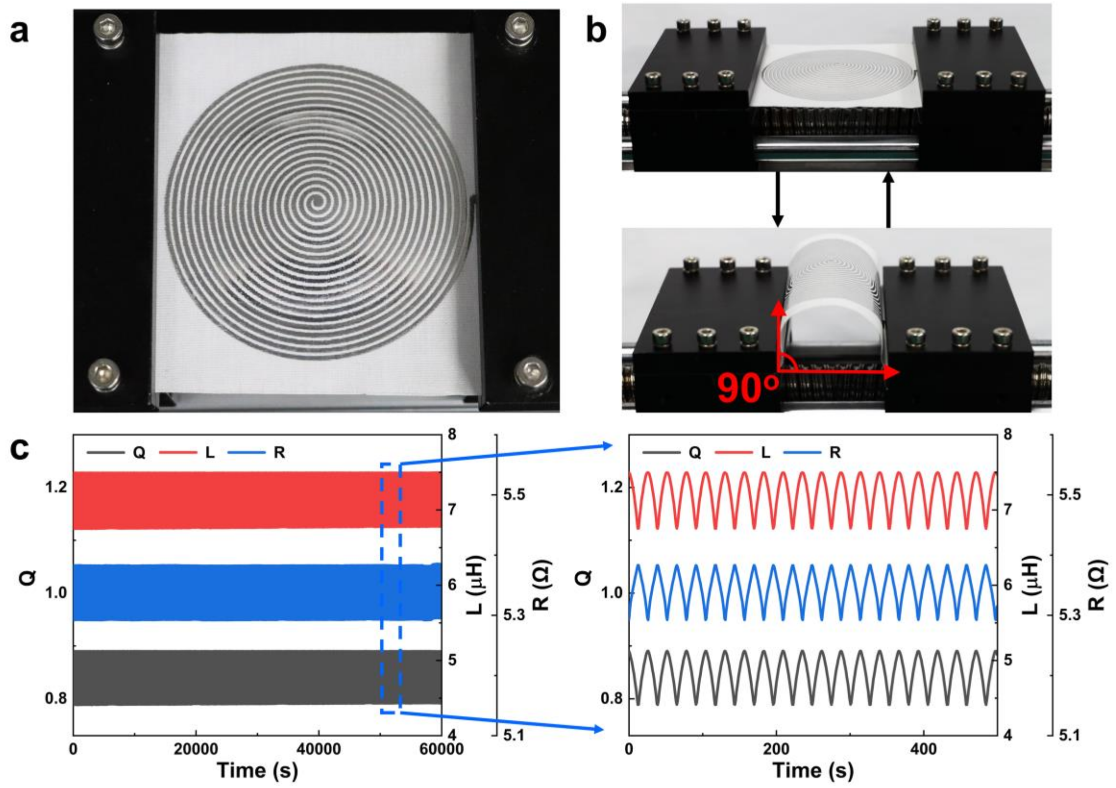

Fig.34| a, Photograph of the receiver coil on cloth fabric. **b,** bending test platform. **c,** the impacts of bending on the electrical resistance (*R*), inductor (*L*), and inductor quality (*Q*) of the receiver coil.

Fig.35| The spiral-shaped transmission coil, winding with a flexible tube filled with the room-temperature liquid metal of GaInSn, is woven into the back of the chair.

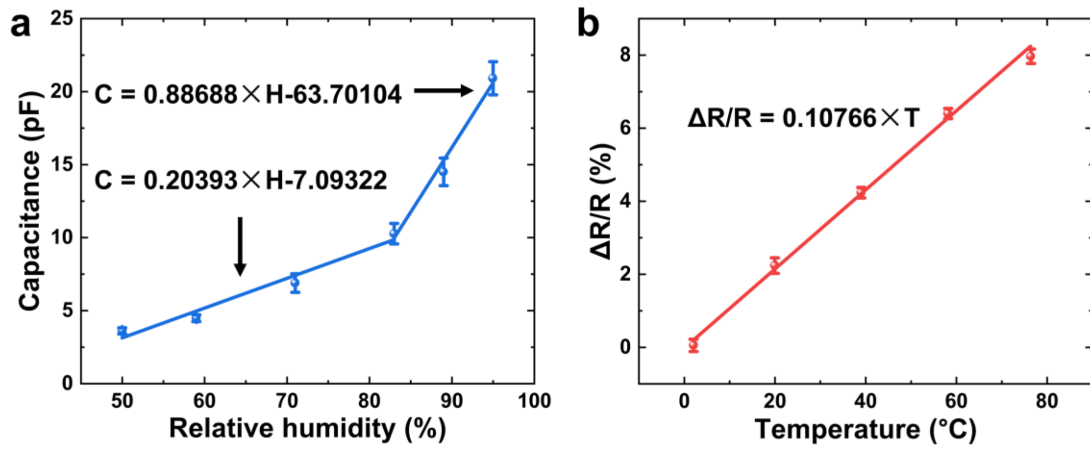

Fig.36| a, The fitting curve of relative humidity-capacitance (n = 4; independent samples). **b,** the fitting curve of temperature-resistance change rate (n = 4; independent samples).

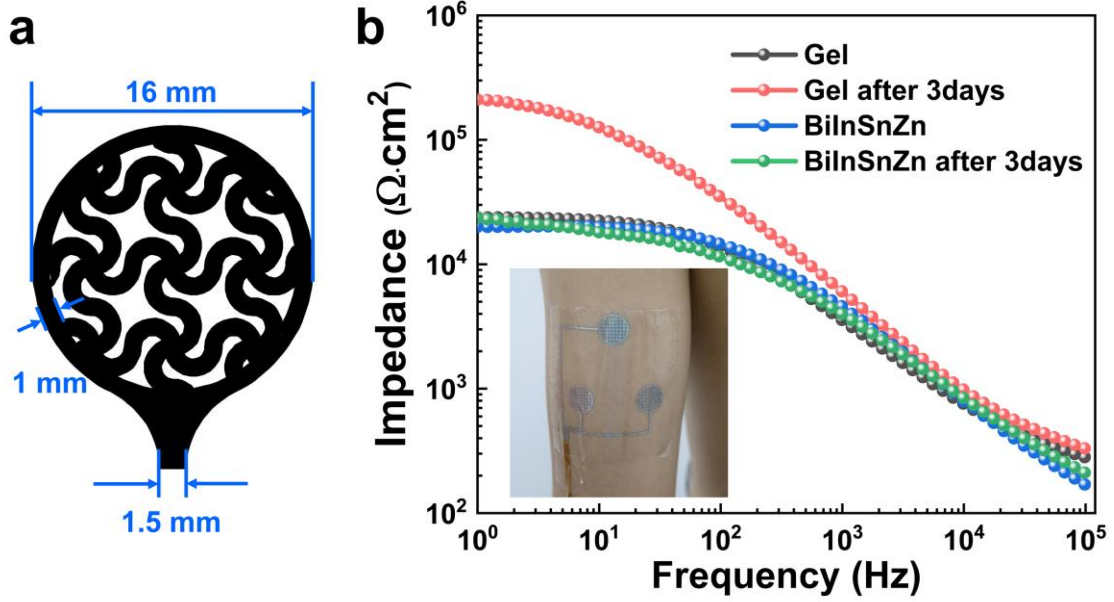

Fig.37| a, The geometry structure of the BiInSnZn electrode. **b,** the impedance under different frequencies for electrodes of BiInSnZn and conductive gel.

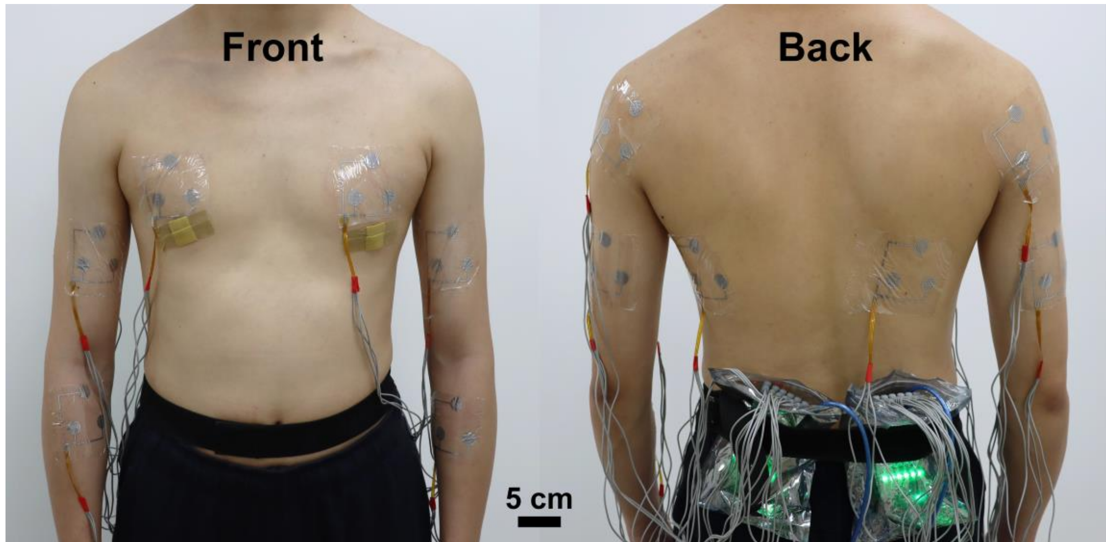

Fig.38| The skin electrode of BiInSnZn for monitoring SMEG signal, inducing complicated electrode routing.

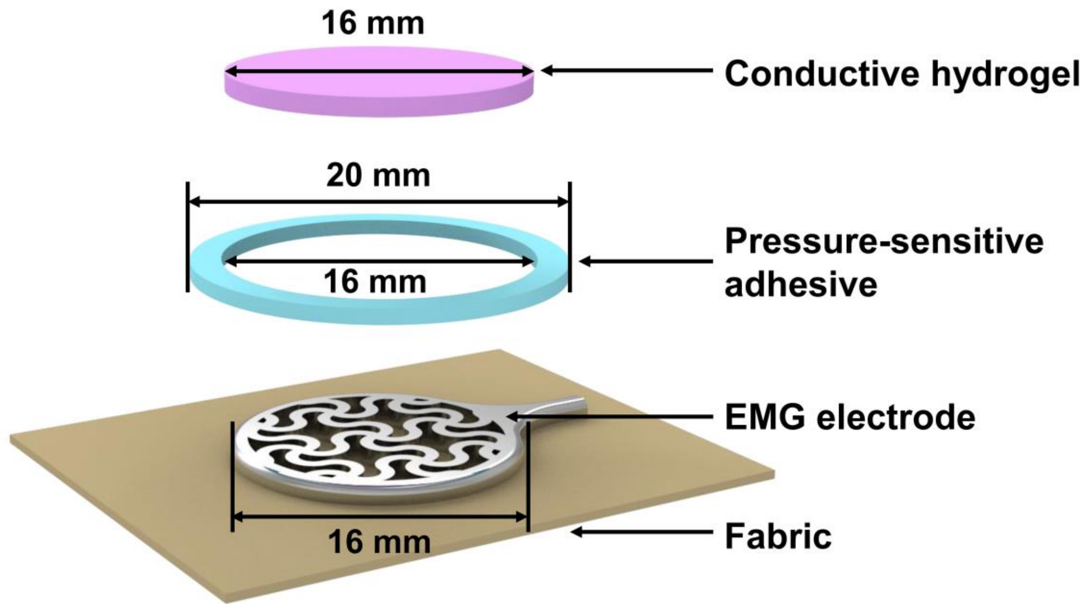

Fig.39| The SMEG electrode structure of BiInSnZn on the textile fabric. The pressure-sensitive adhesive was spin-coated onto a release film at 1500 rpm for 90 s and cured in a drying oven (50°C, 4h). The circular pressure-sensitive adhesive (inner diameter 16 mm, outer diameter 20 mm) cut by a laser cutter (LHC0130, HGTECH) was removed from the release film and adhered around the EMG electrodes. The conductive hydrogel was pasted on top of the EMG electrodes.

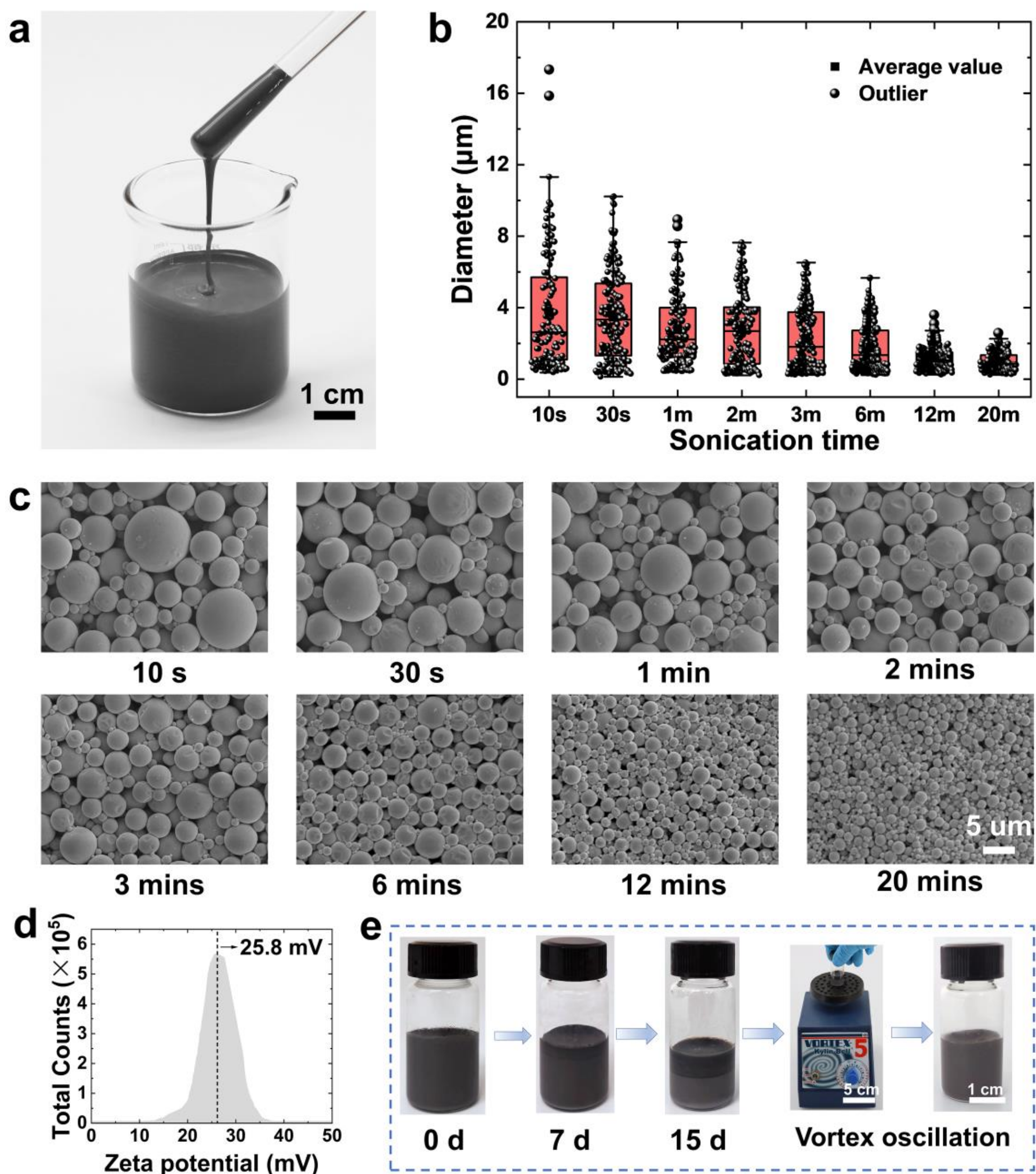

Fig.40| BiInSnZn ink preparation and dispersion stability. a, Photograph of the BiInSnZn ink (microparticle concentration: 4:1 and PVA content 1 wt.%). **b,** Sonication time impacts on the BiInSnzn particle sizes. **c,** SEMs of the BiInSnZn particles under different sonication times (n = 4; independent samples). **d**, Zeta potential (p=0.014) of the BiInSnzn ink (microparticle concentration: 2:1 and PVA content 1 wt.%). **e**, Dispersion stability testing under different setting times. The solution with precipitated particles is dispersed by vortex oscillation.

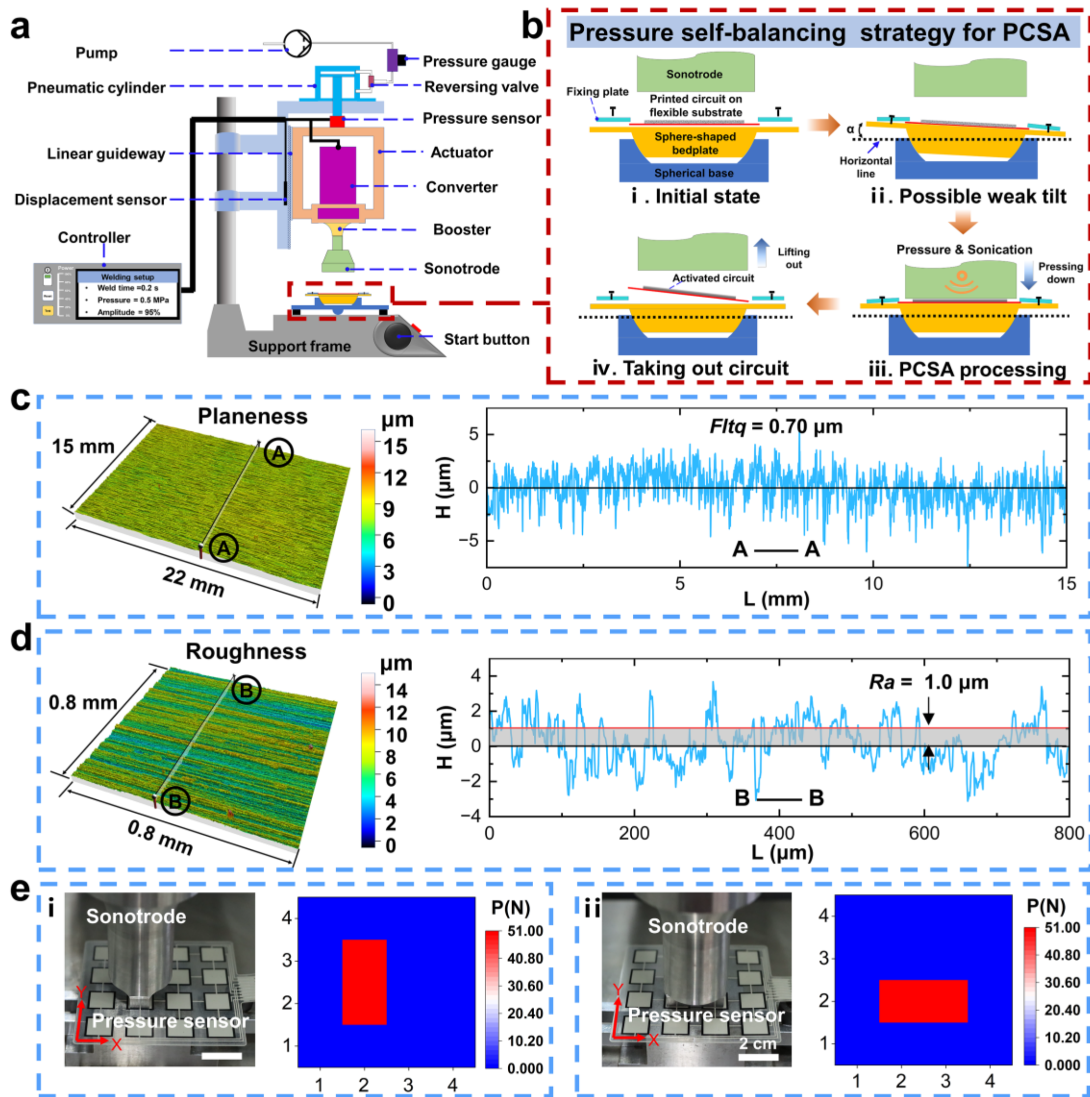

Fig.41| PCSA equipment for printed circuits activation on the flexible substrate. **a,** The working principle of the PCSA equipment. **b**, Pressure self-balancing strategy. **c**, The flatness of the sphere-shaped bedplate surface. **d**, The roughness of the sphere-shaped bedplate surface. **e**, Pressure uniformity of the bedplate surface. (Detailed discussion in Supplementary Note 3).

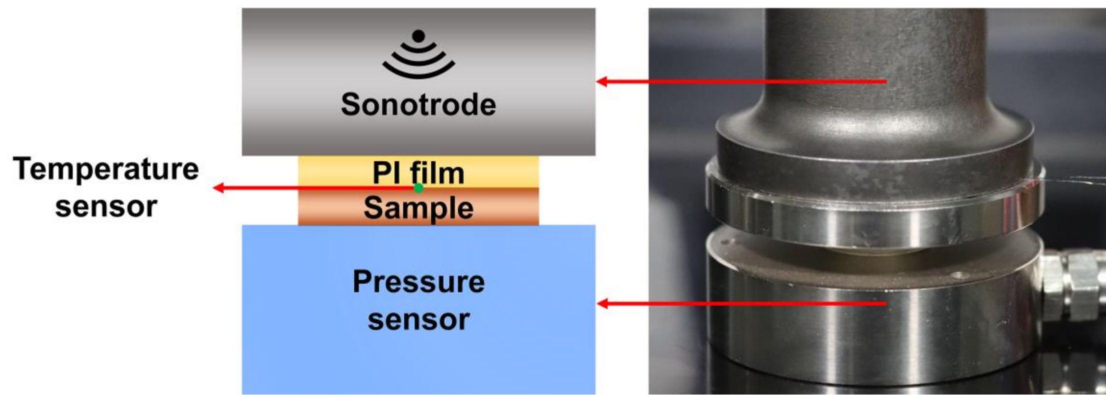

Fig.42| Illustration and photograph of the temperature and dynamical pressure during the PCSA process, the PI film thickness with 50 μm.

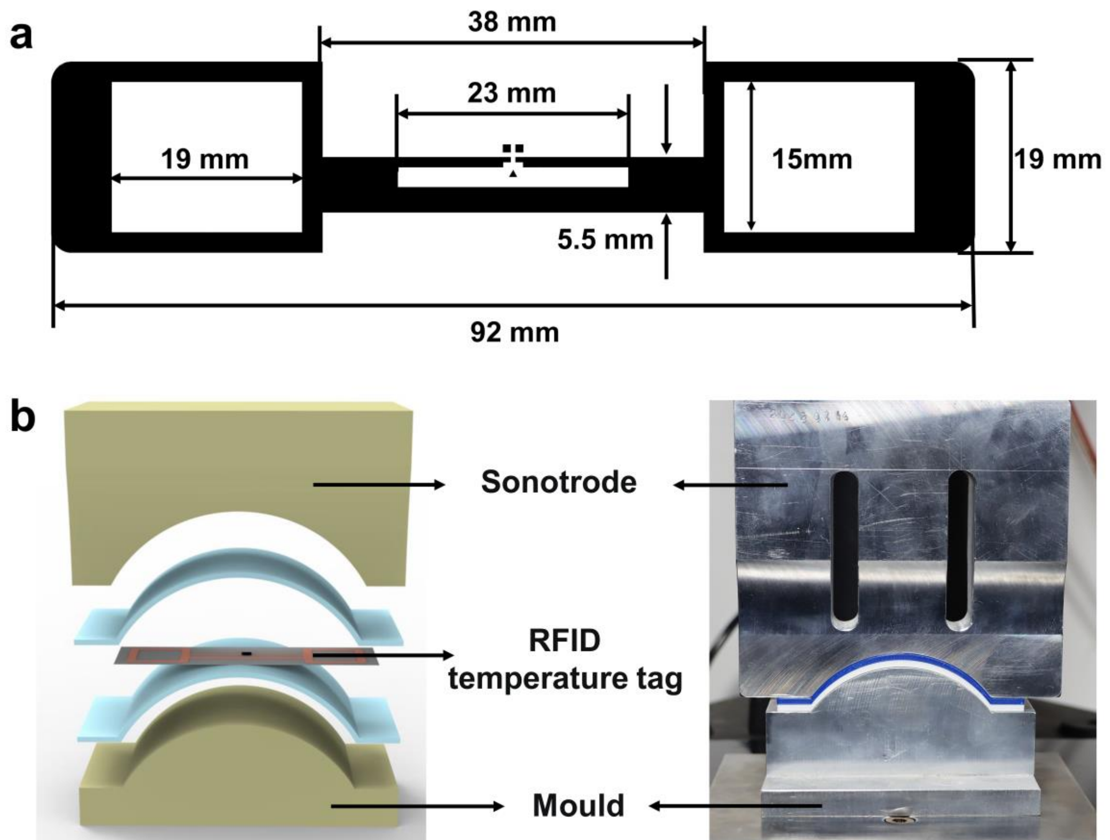

Fig.43| PCSA-based temperature-RFID tag printed on the curved surface. a, the RFID antenna circuit geometry and size. **b,** The RFID antenna is printed on the SBS film and gripped by the 3D-printed structure of acrylonitrile-butadiene-styrene (ABS), which is then activated by the PCSA through an arc-shaped sonotrode.

Fig.44| The FTEG performance test platform: the voltage and current was obtained under different temperature difference of the FTEG cold/hot sides.

Supplementary Table 1. Comparison of posttreatment methods for printed circuits

	TS	LS	IPL	CS	**PCSA**
Particle size	< 100 nm	< 100 nm	< 100 nm	< 100 nm	**less limitation**
Metal melting point	< 1500 ºC	< 1500 ºC	< 1500 ºC	no limitation	**less limitation**
organic ligands for ink	Low boiling point and low content	Low boiling point and low content	Low boiling point and low content	low boiling point and low content	**less limitation**
Flexible substrate	high heat tolerance	low photosensitivity	low photosensitivity	acid corrosion resistance	**less limitation**
Operation condition	> 200 ºC at vacuum or insert gas	room temperature environment	room temperature environment	room temperature environment	**room temperature environment**
Operation time	> 10 mins	< 1 s	< 1 s	> 1 mins	**< 1 s**
Compactness	low	low	low	low	**high**
Efficiency	low	supper low	high	moderate	**high**
Electrical conductivity	moderate	high	high	low	**high**
Interconnecting multilayer circuits	no	no	no	no	**Yes**
Joining electronic components	no	no	no	no	**Yes**

TS: thermal sintering; CS: chemical sintering; IPL: Intense pulsed light sintering; Compactness: particle bonding strength after posttreatment.

Table 1 lists the current main posttreatment methods for printed circuits on flexible substrates and comparison with the PCSA developed in this work. Notably, all the items are given in light of the printed pattern on the flexible substrates. For example, the particle size smaller than 100 nm for the TS method is optimal for metal particle sintering due to the flexible substrates (such as PVA and PET) with low glass transition temperatures. In addition, the large particle radius (> 1 μm) is gently stacked to leave multitudinous holes, which cannot be removed by the existing methods of TS, LS, IPL, and CS.

The working principles of the posttreatment methods:

TS method applies high temperature (>200ºC) under vacuum or inert gas to block more oxidation and induce the decomposition of organic agents and contact fusion between the metal particles.

LS method could generate a hot and small spot to sinter metal particles and enable them to weld with a low penetration depth.

IPL method uses a xenon lamp (broad-spectrum 200~1200 nm) to irradiate printed

patterns and conducts fast sintering within milliseconds under an air environment. It could enable the decomposition of organic agents and the necking of metal particles.

CS method applies acidic solutions to remove organic agents and oxides, enabling clean contacted surfaces of particle sintering.

PCSA method developed in this work could directly deliver the sonication vibration to the particles and induce local high-intensity interaction between them, which makes the particles be reassembled into a dense accumulation, disrupts surface oxidation and coated polymer, and enables their bonding.

Supplementary Table 2. Posttreatment methods for activating printed patterns on the flexible substrate

Ink	Method	Thermal conductivity (W/mK) Operation condition	Particle sizes	Substrate	Conductivity (10^6×S/m)
Ag	CS[1]	Treatment by poly(acrylic acid)	11.1 nm	paper	14.7
	TS[2]	140 °C for 50 mins	48 nm	paper	21.7
	PS[3]	Ambient air and time< 1 s	micro-flakes 2–15 µm	PET	13.3
	PJS[4]	Ambient air and for 50 mins	30-50 nm	paper	1.40
	PCSA	**Ambient air and Time< 1s**	**1 µm**	**paper**	**40.80**
Cu	TS[5]	170 °C under ambient atmosphere for 10 mins	10 µm	PI	1.34
	TS[6]	150 °C under ambient atmosphere	300 nm	PI	1.80
	TS[7]	Vacuum oven cured at 400 °C for 30 mins	400 nm	Si wafers	3.70
	TS[8]	150 °C under N_2 atmosphere	3.5 nm	PI	3.30
	TS[9]	325 °C under vacuum	35-60 nm	PI	8.69
	TS[10]	250 ℃ under N_2 atmosphere	135 nm	PI	6.30
	TS[11]	Coating coordination polymers 250 ℃ under ambient atmosphere and time ≈ 1 min for 50 nm, 2 min for 200 nm	50 nm	PI	22.22
			200 nm	PI	9.00
	IPL[12]	Ambient air	36 nm	PI	10.48
	IPL[13]	Ambient air	2 µm	PI	1.25
	IPL[14]	Ambient air	100 nm	PI	14.00
	IPL[15]	Ambient air	64.6 nm	PET	1.00
	CS[16]	Ambient air at 60 °C and Time<1 min	500 nm	PET	1.34
	PCSA	**Ambient air and Time< 1s**	**1 µm**	**paper**	**30.03**
Zn	LS[17]	Ambient air and argon enclosure	65-75 nm	Transparent Na-CMC	1.10
	PS[18]	Argon environment, time<1 s	135 nm	Transparent Na-CMC	0.45
	CS[19]	Ambient air 90% humidity within 300 mins	170 nm	PVA	0.72
	CS[20]	Acetic aid and Time>1 min	1~5 µm	PLGA	0.30
	CS[21]	Acetic aid and Time>1 min	40-60 nm	PET	0.10
	PCSA	**Ambient air and Time< 1s**	**1 µm**	**paper**	**9.11**
Mo	CS[22]	Propionic anhydrides, 90% humidity	1 µm	PLGA	2.5×10^{-3}
	CS[23]	Treatment with CH_3COOH	10 µm	PLGA	6×10^{-4}
	LS[24]	Ambient air	1.5 µm	PVA	7×10^{-2}
	TS[25]	250 °C for 20 mins	1-5 µm	Glass	10^{-3}
	PCSA	**Ambient air and Time< 1s**	**5 µm**	**paper**	**1.91**
W	CS[21]	Propionic anhydrides, 90% humidity	1 µm	PLGA	1.5×10^{-3}
	CS[26]	Ambient air and for 10-20 mins	4-6 µm	Glass	4×10^{-2}
	CS[27]	Treatment by ethanol and water at 37 °C	6 µm	Glass	5×10^{-3}
	PCSA	**Ambient air and Time< 1s**	**5 µm**	**paper**	**0.67**
Ag_2Se	HP[28]	230 °C and 5 MPa for 5 mins	48 nm	PI	0.10
	HP[29]	200 °C and 1 MPa for 30 mins	50-500 nm	PA	0.09
	HP[30]	200 °C and 1 MPa for 30 mins	60-100 nm	PA	0.09
	HP[31]	200 °C and 1 MPa for 30 mins	65 nm	PA	0.05
	PCSA	**Ambient air and Time< 1s**	**100 nm**	**paper**	**0.13**

PJS: plasma jet sintering; HP: hot pressing.

Supplementary Table 3. Optimal operating parameters for different materials

	Ga, In, Sn, Bi, Zn, Mg, Al, Ag (<1000℃)	Cu, Ni, Co, Fe, Ti, Pt, V (1000~2000℃)	Nb, Mo, Ta, Re, W (>2000℃)
P_s	0~0.4 MPa	0.3~0.5 MPa	~0.5 MPa
t_a	0.05~0.5 s	0.1~0.8 s	0.6~1 s
S_p	1~32 W/cm^2	8~32 W/cm^2	~32 W/cm^2

Supplementary Note 1| PCSA-enabled printed-pattern densification

The lack of an additional driving force in most posttreatment methods leads to the inability to effectively remove a significant number of pores between particles, as demonstrated in Supplementary Fig. 1. Although transient thermal shock, such as a laser pulse, can decompose the coated polymer to enhance close particle contact, it cannot guarantee random close packing, especially for particles with irregular shapes and varying sizes. The thermal (or chemical) effects induce the growth of interparticle junctions at the contact area to form a conductive path; however, this process cannot effectively fill gaps between particles. Our experiment results (Supplementary Fig. 1), which utilized both thermal and laser sintering methods, also confirmed this issue of low densification.

The PCSA method, unlike existing posttreatment methods, achieves excellent electrical conductivity due to its unique densification mechanisms of vibration-induced particle rearrangement and softening-driven compatible plastic deformation, as discussed in the following.

i. **Vibration-enabled densification.** The ultrasonic vibration facilitates particle rearrangement[32-34] under low constraint pressure during the initial stage of the PCSA process, leading to random close packing. This increases the contact area between particles and enhances electrical conduction in printed patterns. The densification enabled by this vibration is primarily responsible for reducing electrical resistances in printed circuits of graphene (GR) inks, as interparticle bonding cannot occur during the PCSA process. The thickness of the printed GR electrode could decrease from 7.28 μm initially to 2.02 μm after the PCSA process, leading to an 87.7% reduction in electrical resistance (Supplementary Fig. 5), demonstrating the mechanism of densification facilitated by vibration.

ii. **Plastic deformation-enabled densification.** The vibration-assisted heating-induced softening and plastic deformation of particles can significantly enhance the densification of the printed pattern during the PCSA process, particularly for metal inks. The vibration-assisted random close packing facilitates efficient transmission

of ultrasonic energy to the printed particles, resulting in high-frequency friction at the particle interface and subsequent heat-softening effects. Consequently, compatible plastic deformation effectively reduces interparticle gaps[34]. The thickness of the printed Cu-microparticle electrode could decrease from an initial value of 14.25 μm to 6.16 μm after undergoing the PCSA process, achieving excellent electrical conductivity of 3.03×10^7 S/m (Supplementary Fig. 1). This benefits from a synergistic mechanism enabled by vibration and plastic deformation that enhances densification, which is also demonstrated by real-time observation of particle microstructure densification evolution (Supplementary Figs. 12 and 13). However, the thermal and laser sintering methods are insufficient for achieving high densification, especially with larger particles (radius>1 μm), leading to low stacking density and inadequate conductivity.

Supplementary Note 2| Details of finite element simulation

Finite element simulations are conducted using the commercial package Abaqus/Explicit 2020 to analyze the entire process of PCSA, which involves three stages (as illustrated in Fig. 1a of the text). However, due to the complex multi-scale physical interaction, it is challenging to employ numerical simulation methods. As an alternative approach, we used three 2D simulation models to emphasize the effects of coated PVA polymer on PCSA performance (Case I in Supplementary Movie 5 and Supplementary Fig. 8), particle-particle interaction (Case II in Supplementary Movie 5 and Supplementary Fig. 14), and particle mechanical properties (Case III in Supplementary Movie 5 and Supplementary Fig. 19), respectively. These models were utilized to explain experimental observations.

i. Suppressing particle segregation (Case I in Supplementary Movie 5 and Supplementary Fig. 8)

The Johnson-Cook intrinsic structure relation is used to describe the plastic deformation behavior of the Cu particle, denoted as[35]

$$\sigma=\left(A+B\varepsilon_e^n\right)\left(1+C\ln\frac{\dot{\varepsilon}}{\dot{\varepsilon}_0}\right)\left[1-\left(\frac{T-T_0}{T_m-T_0}\right)^m\right] \tag{1}$$

where the equivalent plastic strain ε_e is defined as the ratio of the accumulated plastic deformation to the initial volume, $\dot{\varepsilon}_0 = 1\text{s}^{-1}$ is the reference strain rate. The temperatures $T_0 = 20^\circ\text{C}$ and $T_m = 1084.8^\circ\text{C}$ are taken as references for ambient and melting conditions of copper, respectively. Material-related constants A = 352.1 MPa, B = 267.5 MPa, and C = 0.0318 are utilized in conjunction with parameters n = 0.5299 and m = 0.6814 to account for strain-hardening and thermal-softening effects, respectively; furthermore, additional material properties such as density (8960 kg/m^3), thermal conductivity (377 W/mK), specific heat (383 J/kgK) are also considered for copper specimens under investigation herein. Finally, a thin layer of polyvinyl alcohol (PVA) coating with thickness of 50 nm (see Supplementary Fig. 8c) was applied on top of the specimen surface; its mechanical properties[36] were characterized by Young's modulus E = 1 GPa

and Poisson's ratio $v = 0.331$.

The sonotrode vibration has a frequency of 20 kHz and an amplitude of 0.2 μm. As depicted in Supplementary Fig. 8c, the distance between the centroid points of the upper and lower particles is utilized to characterize their mutual position, initially measured as H_0=0.866 μm for a particle diameter of 1 μm. During PCSA postprocessing without coated PVA polymer, the sonotrode induces elastic deformation (accompanied by slight plastic deformation) in micro/nanoparticles at the initial stage. At the lowest point of downward pressuring on the sonotrode (corresponding to 12.5 μs, see Supplementary Fig. 8c), particle elastic deformation results in H/H_0=0.9. Subsequently, as shown in Supplementary Fig. 8c, after lifting out the sonotrode (at around 20 μs), accumulated elastic energy converts into kinetic energy and causes aimless particle flight with H/H_0 >1. Simulation results also indicate that sonication vibration triggers inter-particle elastic collisions without interfacial adhesion and initiates particle segregation during early stages. The presence of coated PVA introduces plastic deformation at particle interfaces, which enhances energy dissipation, leading to inelastic collisions and suppressing particle segregation under sonication vibration conditions (Supplementary Figs. 8d and e). Due to significant plastic deformation occurring within the PVA layer between particles, the coated-PVA thickness decreases from 100 nm to 50 nm, therefore maintaining H/H_0 <1 when subjected to cyclic loading.

ii. **Particle interface friction (Case II in Supplementary Movie 5 and Supplementary Fig. 14)**

The particles of BiInSnZn and Cu are examined in this study to investigate the friction at particle interfaces (Supplementary Fig. 14) for supporting experimental observations. A modified Johnson-Cook model is employed to account for the effects of strain-softening and strain rate-temperature coupling in BiInSnZn. The flow stress $\sigma=\sigma_s+S$ is decomposed into a transient flow resistance S and a steady state plateau stress σ_s, which are modeled separately[37]. All the relevant parameters are estimated based on the results of mechanical experiments (Supplementary Fig. 14). The steady-state plateau stress σ_s follows the Johnson-Cook model:

$$\sigma_s = A\left(1 + C_1 \ln\frac{\dot{\varepsilon}}{\dot{\varepsilon}_0}\right)\left[1 - \left(\frac{T - T_0}{T_m - T_0}\right)^{m_1}\right] \tag{2}$$

where A=15.9651 MPa, C_1=0.002 and m_1=8.3009 are adopted for BiInSnZn. The transient flow resistance S is modeled differently, considering that the initial softening-slope $dS/d\varepsilon$ is constant at t = 0. Using a differential equation to predict the evolution of S:

$$\dot{S} = -h_0 \dot{\varepsilon} \frac{S}{S_0} \tag{3}$$

where h_0=20.4357 MPa is the initial-softening-slope. The initial resistance S_0 follows the Johnson-Cook model:

$$S_0 = \overline{S_0}\left(1 + C_2 \ln\frac{\dot{\varepsilon}}{\dot{\varepsilon}_0}\right)\left[1 - \left(\frac{T - T_0}{T_m - T_0}\right)^{m_2}\right] \tag{4}$$

where $\overline{S_0}$, C_2=0.0903, and m_2=12.9722. In addition, the material properties of BiInSnZn[38] include density (7900 kg/m^3), thermal conductivity (19.2 W/mK), and specific heat (270 J/kgK).

The vibration amplitude of the sonotrode is set to 0.05 μm, and considering the plastic deformation of the BiInSnZn particles, the original position of the sonotrode is reduced by 0.02 μm per cycle to simulate realistic experimental conditions. The vibration amplitude of the sonotrode is adjusted to 0.3 μm for Cu particles, and the original position of the acoustic probe is decreased by 0.05 μm per cycle. The tangential friction coefficient for Cu particle contact is 0.7, while it is 0.4 for BiInSnZn particles. We conduct three simulation cycles and monitor the peak temperature at the interface between particles.

The simulation results demonstrate that high-frequency friction can generate localized peak temperatures (approaching or even exceeding the melting point of BiInSnZn) at the particle interface (Supplementary Fig. 14a), leading to heat-softening effects and facilitating particle bonding under low constraint pressure. A substantial increase in peak temperature (approximately 195°C) enhances surface activation energy and atomic diffusion between particles (Supplementary Fig. 14b). This enables

rapid welding of particles and strong binding with neighboring particles. The peak temperature rapidly decreases due to heat absorption by particles and weakened interaction caused by plastic deformation, resulting in minimal damage to flexible substrates.

iii. **Impacts of the metal particle mechanical properties (Case III in Supplementary Movie 5 and Supplementary Fig. 19)**

Three types of metal particles (BiInSnZn, Cu, and W) coated with oxide layers (SnO_2, CuO, and WO_3) having a thickness of 50 nm are considered for characterizing the influence of mechanical properties on activation performance (Supplementary Fig. 19). The deformation of particles was assessed using logarithmic strain (LE),

$$LE = \int_{l_0}^{l_1} \frac{dl}{l} = \ln \frac{l_1}{l_0} \tag{5}$$

where l is the instantaneous length, l_0 is the initial length, and l_1 is the ending length. The fracture parameters for SnO_2 (density of 6900 kg/m^3, Young's modulus of 80 GPa, and Poisson ratio of 0.433), CuO (6400 kg/m^3, 658 GPa, and 0.442), and WO_3 (7160 kg/m^3, 150 GPa, and 0.4)[39] are selected using the same criteria.

The simulations have demonstrated (Supplementary Fig. 19) that the metal of W (Young’s Modulus: 411 GPa, T_m=3422°C) requires a higher pressure to fracture its oxide layer compared to the softened metals of BiInSnZn (Young’s Modulus: 12 GPa, T_m=60°C) and Cu (Young’s Modulus: 110 GPa, T_m=1084.8°C). It is observed that different pressing forces of 9.8 μN, 161 μN, and 967 μN are necessary to completely break the oxide layers for BiInSnZn, Cu, and W, respectively. This indicates that metals with lower Young's modulus require less pressure to destroy the oxide layer on their surface particles. However, low-constrained pressure is employed in PCSA processing to minimize heat generation on flexible substrates. The high melting temperature of metal particles contributes to their higher hardness, which results in heat softening-induced plastic deformation occurring at elevated temperatures. These simulation findings align with experimental observations indicating that lower metal particle hardness leads to increased activated electrical conductivities (Supplementary Fig. 18).

Supplementary Note 3| Working principle of the PCSA equipment

Compared to bulk material welding by sonication, careful design of the PCSA is necessary to achieve high interface mechanical compatibility for flexible substrates printed with particle-based patterns of thin thickness. The working principle of our PCSA equipment is illustrated in Supplementary Fig. 42a. Pneumatic pressure facilitates the pressing of the sonotrode onto the flexible substrate. Once the contact pressure reaches a pre-set value, the sonotrode delivers rapid sonication vibration to activate the printed circuits on the flexible substrate (within a second). To ensure uniform constrained pressure over large areas on flexible substrates, we employ a pressure self-balancing strategy during the PCSA process, as depicted in Supplementary Fig. 42b. A sphere-shaped bedplate is fixed onto a spherical base coated with lubricating oil, allowing relative motion between them. When there is a slight tilting of the sphere-shaped bedplate, contact pressure from sonication triggers its motion to maintain uniform loaded pressure on flexible substrates.

Another crucial aspect is maintaining a high level of flatness and roughness on the surface of the sphere-shaped bedplate, which can be achieved through precision polishing. We measured the flatness error and surface roughness of these bedplates. The flatness error is scanned within the 15 mm × 22 mm sweep region, while the surface roughness is evaluated in the 0.8 mm × 0.8 mm sweep region, as depicted in Supplementary Fig. 42c and Supplementary Fig. 42d, respectively. Flatness is assessed using the root mean square flatness deviation (Fltq),

$$Fltq = \sqrt{\frac{1}{A}\int_A d^2 dA} \tag{1}$$

where d is the local flatness deviation, and A is the flatness area of the geometric element. The flatness error of the obtained scanning plane is only 0.7 μm. Roughness was assessed with the contour arithmetic mean deviation (Ra), expressed as

$$Ra = \frac{1}{l}\int_0^l \left|H(x)\right| dx \tag{2}$$

where l is the sampling length, and $H(x)$ is the absolute values of the longitudinal coordinates of the contour points. The roughness of the obtained scanning plane is only

1 μm. The high surface flatness and low roughness, combined with the pressure self-balancing strategy, ensure uniform contact between the bedplate and the sonotrode. As illustrated in Supplementary Fig. 42e, the thin-film array pressure sensor unit experiences a consistent pressure of 51 N in both X and Y directions. The uniformity of constrained pressure in the PCSA process promotes even activation of the large-area circuit.

Reference

1 Magdassi, S., Grouchko, M., Berezin, O. & Kamyshny, A. Triggering the Sintering of Silver Nanoparticles at Room Temperature. Acs Nano 4, 1943-1948, doi:10.1021/nn901868t (2010).

2 Mo, L. X. et al. Nano-Silver Ink of High Conductivity and Low Sintering Temperature for Paper Electronics. Nanoscale Res Lett 14, 197, doi: 19710.1186/s11671-019-3011-1 (2019).

3 Cui, H. W. et al. Ultra-fast photonic curing of electrically conductive adhesives fabricated from vinyl ester resin and silver micro-flakes for printed electronics. Rsc Adv 4, 15914-15922, doi:10.1039/c4ra00292j (2014).

4 Turan, N. et al. Atmospheric Pressure and Ambient Temperature Plasma Jet Sintering of Aerosol Jet Printed Silver Nanoparticles. Acs Appl Mater Inter 13, 47244-47251, doi:10.1021/acsami.1c14049 (2021).

5 Hong, S. Q. et al. Antioxidant high-conductivity copper paste for low-cost flexible printed electronics. Npj Flex Electron 6, 1710, doi: 1038/s41528-022-00151-1 (2022).

6 Kanzaki, M., Kawaguchi, Y. & Kawasaki, H. Fabrication of Conductive Copper Films on Flexible Polymer Substrates by Low-Temperature Sintering of Composite Cu Ink in Air. Acs Appl Mater Inter 9, 20852-20858, doi:10.1021/acsami.7b04641 (2017).

7 Teo, B. H. et al. Development of nanoparticle copper screen printing pastes for silicon heterojunction solar cells. Sol Energy 189, 179-185, doi:10.1016/j.solener.2019.07.055 (2019).

8 Hokita, Y., Kanzaki, M., Sugiyama, T., Arakawa, R. & Kawasaki, H. High-Concentration Synthesis of Sub-10-nm Copper Nanoparticles for Application to Conductive Nanoinks. ACS Appl Mater Interfaces 7, 19382-19389, doi:10.1021/acsami.5b05542 (2015).

9 Jeong, S. et al. Controlling the Thickness of the Surface Oxide Layer on Cu Nanoparticles for the Fabrication of Conductive Structures by Ink-Jet Printing. Advanced Functional Materials 18, 679-686, doi:10.1002/adfm.200700902 (2008).

10 Zhang, Y. et al. Facile preparation of monodisperse, impurity-free, and antioxidation copper nanoparticles on a large scale for application in conductive ink. ACS Appl Mater Interfaces 6, 560-567, doi:10.1021/am404620y (2014).

11 Wang, L. et al. Antioxidant High-Conductivity Copper Pastes Based on Core–Shell Copper Nanoparticles for Flexible Printed Electronics. Advanced Functional Materials 33, doi:10.1002/adfm.202215127 (2023).

12 Kim, J. et al. Simple, Fast, and Scalable Reverse-Offset Printing of Micropatterned Copper Nanowire Electrodes with Sub-10 mu m Resolution. Acs Appl Mater Inter 14, 5807-5814, doi:10.1021/acsami.1c21223 (2022).

13 Joo, S. J., Hwang, H. J. & Kim, H. S. Highly conductive copper nano/microparticles ink via flash light sintering for printed electronics. Nanotechnology 25, 265601, doi:10.1088/0957-4484/25/26/265601 (2014).

14 Hwang, Y. T., Chung, W. H., Jang, Y. R. & Kim, H. S. Intensive Plasmonic Flash Light Sintering of Copper Nanoinks Using a Band-Pass Light Filter for Highly Electrically Conductive Electrodes in Printed Electronics. ACS Appl Mater Interfaces 8, 8591-8599, doi:10.1021/acsami.5b12516 (2016).

15 Ankireddy, K. *et al.* Seed mediated copper nanoparticle synthesis for fabricating oxidation free interdigitated electrodes using intense pulse light sintering for flexible printed chemical sensors. *Journal of Materials Chemistry C* 5, 11128-11137, doi:10.1039/c7tc03522e (2017).

16 Sarwar, N. et al. Synthesis of citrate-capped copper nanoparticles: A low temperature sintering approach for the fabrication of oxidation stable flexible conductive film. Appl Surf Sci 542, 148609, doi: 14860910.1016/j.apsusc.2020.148609 (2021).
17 Shou, W. et al. Low-Cost Manufacturing of Bioresorbable Conductors by Evaporation-Condensation-Mediated Laser Printing and Sintering of Zn Nanoparticles. Adv Mater 29, 1700172, doi: 10.1002/adma.201700172 (2017).
18 Mahajan, B. K., Yu, X. W., Shou, W., Pan, H. & Huang, X. Mechanically Milled Irregular Zinc Nanoparticles for Printable Bioresorbable Electronics. Small 13, 1700065, doi:10.1002/smll.201700065(2017).
19 Li, J. M. et al. Anhydride-Assisted Spontaneous Room Temperature Sintering of Printed Bioresorbable Electronics. Adv Funct Mater 30, 1905024, 10.1002/adfm.201905024(2020).
20 Lee, Y. K. et al. Room Temperature Electrochemical Sintering of Zn Microparticles and Its Use in Printable Conducting Inks for Bioresorbable Electronics. Adv Mater 29, 1702665, 10.1002/adma.201702665(2017).
21 Majee, S. et al. Low temperature chemical sintering of inkjet-printed Zn nanoparticles for highly conductive flexible electronic components. Npj Flex Electron 5, 14, doi: 1410.1038/s41528-021-00111-1 (2021).
22 Li, J. M. et al. Fully printed and self-compensated bioresorbable electrochemical devices based on galvanic coupling for continuous glucose monitoring. Sci Adv 9, eadi3839 9, doi: 10.1126/sciadv.adi3839(2023).
23 Lee, Y. K. et al. Room Temperature Electrochemical Sintering of Zn Microparticles and Its Use in Printable Conducting Inks for Bioresorbable Electronics. Adv Mater 29, doi:10.1002/adma.201702665 (2017).
24 Feng, S., Cao, S., Tian, Z., Zhu, H. & Kong, D. Maskless Patterning of Biodegradable Conductors by Selective Laser Sintering of Microparticle Inks and Its Application in Flexible Transient Electronics. ACS Applied Materials & Interfaces 11, 45844-45852, doi:10.1021/acsami.9b14431 (2019).
25 Lee, S. et al. Metal microparticle-Polymer composites as printable, bio/ecoresorbable conductive inks. Materials Today 21, 207-215, doi:10.1016/j.mattod.2017.12.005 (2018).
26 Huang, X. et al. Biodegradable Materials for Multilayer Transient Printed Circuit Boards. Advanced Materials 26, 7371-7377, doi:10.1002/adma.201403164 (2014).
27 Atreya, M. et al. Poly(lactic acid)-Based Ink for Biodegradable Printed Electronics With Conductivity Enhanced through Solvent Aging. ACS Applied Materials & Interfaces 12, 23494-23501, doi:10.1021/acsami.0c05196 (2020).
28 Lee, D. C. et al. Substrate-Free Thermoelectric 25 um-Thick Ag2Se Films with High Flexibility and In-Plane zT of 0.5 at Room Temperature. Acs Appl Mater Inter 15, 3047-3053, doi:10.1021/acsami.2c20115 (2023).
29 Jiang, C. et al. Ultrahigh Performance of n-Type Ag2Se Films for Flexible Thermoelectric Power Generators. Acs Appl Mater Inter 12, 9646-9655, doi:10.1021/acsami.9b21069 (2020).
30 Jiang, C. et al. Ultrahigh performance polyvinylpyrrolidone/Ag2Se composite thermoelectric film for flexible energy harvesting. Nano Energy 80, 105488, doi: 10548810.1016/j.nanoen.2020.105488 (2021).
31 Ding, Y. F. et al. High performance n-type Ag2Se film on nylon membrane for flexible thermoelectric power generator. Nat Commun 10, 841, doi: 84110.1038/s41467-019-08835-5 (2019).
32 G.D. Scott, Packing of spheres: packing of equal spheres, Nature, 1960(188): 908-

909. DOI: 10.1038/188908a0;

33 Yongli Wu, Xizhong An, A.B. Yu, DEM simulation of cubical particle packing under mechanical vibration, Powder Technology, 2017(314):89-101. DOI: 10.1016/j.powtec.2016.09.029.

34 Ward, A. A. et al. Macroscopic yielding and particle-scale densification mechanisms in ultrasonic powder compaction. J Mech Phys Solids 167, 105011 doi:10.1016/j.jmps.2022.105011 (2022).

35 Xu, Z. & Huang, F. Comparison of constitutive models for FCC metals over wide temperature and strain rate ranges with application to pure copper. International Journal of Impact Engineering 79, 65-74, doi:10.1016/j.ijimpeng.2014.10.003 (2015).

36 Morimune-Moriya, S., Goto, T. & Nishino, T. Effect of aspect ratio of graphene oxide on properties of poly (vinyl alcohol) nanocomposites. Nanocomposites 5, 84-93, doi:10.1080/20550324.2019.1647688 (2019).

37 Nguyen, Q. K., Deng, F. & Zhang, P. Temperature and rate dependent constitutive behaviors of low melt Field’s metal. Extreme Mech Lett 37, 100697 doi:10.1016/j.eml.2020.100697 (2020).

38 Yang, X. H. et al. Experimental and numerical investigation of low melting point metal based PCM heat sink with internal fins. Int Commun Heat Mass 87, 118-124, doi:10.1016/j.icheatmasstransfer.2017.07.001 (2017).

39 Feng, Y. C. et al. Fabrication and characteristic of Al-based hybrid composite reinforced with tungsten oxide particle and aluminum borate whisker by squeeze casting. Mater Design 29, 2023-2026, doi:10.1016/j.matdes.2008.04.006 (2008).